Biochemistry

pubs.acs.org/biochemistry Article

Revisiting the Burden Borne by Fumarase: Enzymatic Hydration of an Olefin

Asutosh Bellur,[▽] Soumik Das,[▽] Vijay Jayaraman, Sudarshan Behera, Arpitha Suryavanshi, Sundaram Balasubramanian, Padmanabhan Balaram, Garima Jindal,* and Hemalatha Balaram*

Cite This: *Biochemistry* 2023, 62, 476−493 Read Online

ACCESS | Metrics & More | Article Recommendations | Supporting Information

ABSTRACT: Fumarate hydratase (FH) is a remarkable catalyst that decreases the free energy of the catalyzed reaction by 30 kcal mol^{-1}, much larger than most exceptional enzymes with extraordinary catalytic rates. Two classes of FH are observed in nature: class-I and class-II, which have different folds, yet catalyze the same reversible hydration/dehydration reaction of the dicarboxylic acids fumarate/malate, with equal efficiencies. Using class-I FH from the hyperthermophilic archaeon *Methanocaldococcus jannaschii* (Mj) as a model along with comparative analysis with the only other available class-I FH structure from *Leishmania major* (Lm), we provide insights into the molecular mechanism of catalysis in this class of enzymes. The structure of MjFH apo-protein has been determined, revealing that large intersubunit rearrangements occur across apo- and holo-protein forms, with a largely preorganized active site for substrate binding. Site-directed mutagenesis of active site residues, kinetic analysis, and computational studies, including density functional theory (DFT) and natural population analysis, together show that residues interacting with the carboxylate group of the substrate play a pivotal role in catalysis. Our study establishes that an electrostatic network at the active site of class-I FH polarizes the substrate fumarate through interactions with its carboxylate groups, thereby permitting an easier addition of a water molecule across the olefinic bond. We propose a mechanism of catalysis in FH that occurs through transition-state stabilization involving the distortion of the electronic structure of the substrate olefinic bond mediated by the charge polarization of the bound substrate at the enzyme active site.

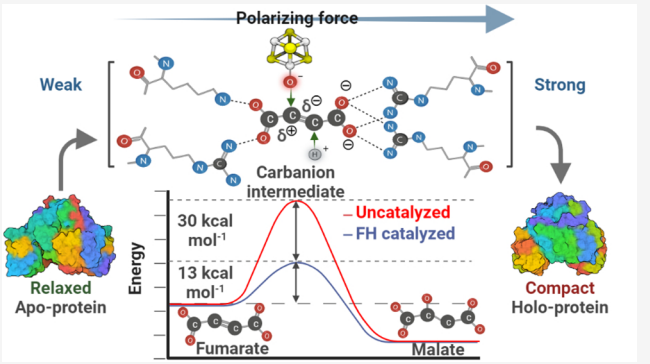

INTRODUCTION

Fumarate, a symmetric olefinic dicarboxylic acid, is an important intermediate in the tricarboxylic acid (TCA, Krebs') cycle. In living cells, fumarate is efficiently and stereospecifically converted to L-malate in a hydration reaction, catalyzed by the enzyme fumarate hydratase (fumarase, FH, E.C. 4.2,1.2). Yet, in organic chemistry, olefin hydration presents many challenges,[1−3] leading to the provocative conclusion that "enzymes are the best chemists".[1] On the scale of "enzyme proficiency," which is the ratio of the rates of the enzyme-catalyzed and -uncatalyzed reactions in aqueous solution, fumarase (FH) ranks high with a 10^{15}-fold rate enhancement in the enzymatic reaction. The 36 kcal mol^{-1} activation barrier, which must be surmounted for catalysis, has been described, by Bearne and Wolfenden, as the "burden borne by fumarase."[4] The biochemical equilibrium in the reversible hydration reaction in the TCA cycle lies in the direction of malate (K_{eq} = 4, first measured by Krebs),[5,6] suggesting that the rates of hydration are 4-fold higher than the rates of dehydration.[7] How does the enzyme lower this formidable activation barrier for this deceptively simple reaction? While kinetic and thermodynamic analyses have provided valuable insights, the molecular mechanisms remain to be clarified.[7,8]

Fumarate hydratases (FHs) are distinctly divided into two classes, class-I and class-II, based on the presence or absence of a 4Fe−4S cluster, respectively.[9] Both classes of FHs are ubiquitous across all kingdoms of life. While class-II enzymes occur predominantly in eukaryotes, class-I enzymes are widely distributed across archaea and prokaryotes, with sparse representation in eukaryotes.[10] These two enzymes share no sequence or structural similarity, yet catalyze the same reaction with close to equal efficiencies.[4,11] There is support for the chemical mechanism in class-II fumarases taking place through all three possible pathways: carbonium (E1),[12] concerted (E2),[13] and carbanion (E1cB)[14] pathways (Scheme 1), with the weight of evidence tilting in favor of the carbanion

Received: September 16, 2022
Revised: December 13, 2022
Published: January 3, 2023

https://doi.org/10.1021/acs.biochem.2c00541
Biochemistry 2023, 62, 476−493

Scheme 1. Mechanisms for Dehydration of Malate to Fumarate[a]

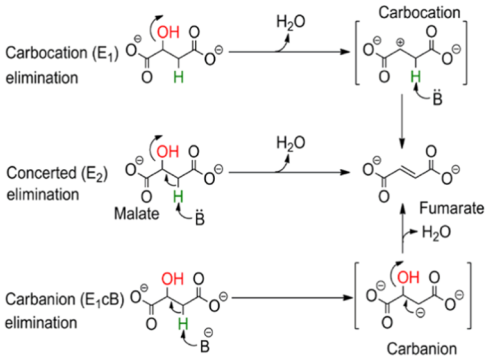

[a]E_1 and E_1cb mechanisms proceed through a two-step reaction involving a carbocation and a carbanion intermediate, respectively, while the E_2 mechanism is a one-step reaction that proceeds without an intermediate with simultaneous removal of a proton and elimination of a water molecule.

pathway.[15] Class-II FHs have been placed under the aspartase/fumarase family of enzymes, which share a common fold. Structural and mechanistic studies have focused on the malate dehydration reaction, with discussion centered on general acid−base catalysis. A conserved serine residue is believed to be the catalytic base, while the catalytic acid has remained elusive in this class of enzymes.[16] Extensive kinetic isotope experiments in class-II FH have revealed that the rate-limiting step of the reaction does not involve a carbon−hydrogen bond breakage or formation. The rate-limiting step is thought to be either the product release or proton exchange alongside a slow conformational isomerization.[13,17−19]

Unlike class-II fumarases, a comprehensive understanding of enzyme chemistry and catalysis is lacking for class-I FHs due to their thermolabile and oxygen-sensitive nature. Class-I FHs are further divided into single-subunit and two-subunit types, depending on the number of genes coding for the functional enzyme. Two-subunit proteins are found only in prokaryotes and archaea, but not in eukaryotes. The α and β subunits of the two-subunit type class-I FHs correspond to the N-terminal and C-terminal domains (NTD and CTD) of single-subunit class-I FHs.[20] Both these enzymes have high sequence similarity, and a small polypeptide insertion between the two subunits is the only distinguishing feature between them. Single-subunit class-I FHs have been biochemically characterized in a handful of organisms.[10,21−27] Thus far, only two-subunit class-I FHs from *Pelotomaculum thermoprpionicum*[20] and *Pyrococcus furiosus*[28] have been biochemically characterized. The recent report on the structure of a substrate-bound class-I FH from *Leishmania major* is a major step forward in probing the molecular mechanism of the fumarase reaction.[27]

Transition-state stabilization in the fumarase reaction is driven by both enthalpic and entropic factors (ΔH = −24 kcal mol^{-1} and ΔS = 19 cal mol^{-1} K^{-1}).[4] The large enthalpic stabilization probably arises from the electrostatic interactions of the tri-negative aci-carboxylate anion at the substrate binding site, while the positive entropic gain can arise from the liberation of the water solvent shell around the fumarate dianion upon binding to the enzyme active site. Bearne and Wolfenden concluded over 25 years ago that the "nature of enzyme−ligand interactions will be clearer when structural information about this remarkable catalyst becomes available".[4]

In this report, we compare the structure of the apo-form of the thermostable, two-subunit FH from *Methanocaldococcus jannaschi* with *L. major* FH (MjFH and LmFH), probe mutational effects on catalysis using several mutant enzymes, and report density functional theory (DFT) calculations to gain insights into the mechanism of the fumarase reaction. Our results provide strong support for electrostatic stabilization at the active site of a charge-polarized, aci-carboxylate form of fumarate as the transition state in the hydration reaction.

EXPERIMENTAL PROCEDURES

Generation of Plasmid Constructs. The open reading frames for the subunits of MjFHα and MjFHβ were amplified by polymerase chain reaction (PCR) from *M. jannaschii* genomic DNA (procured from ATCC) using primers listed in Table S1 and cloned into two tandem multiple cloning sites of the pET-Duet vector (Novagen, Merck), using the restriction enzymes *Bam*HI and *Sal*I for the MjFHα subunit, and *Nde*I and *Xho*I for the MjFHβ subunit such that they can be coexpressed from the same plasmid (pETduet_MjFH$\alpha\beta$). For expressing the individual subunits separately, the same primers and restriction sites were used. Site-directed mutants were generated using the PCR-driven overlap extension method using pETduet_MjFH$\alpha\beta$ as a template. DNA fragments with the required mutations, generated using appropriate oligonucleotides were then assembled into the plasmid by ligation-dependent cloning.[29] All of the clones were confirmed by DNA sequencing.

Protein Expression, Purification, and Reconstitution of an Iron−Sulfur Cluster. Recombinant MjFH$\alpha\beta$ (UniProt Accession ID, α-subunit: Q58690, β-subunit: Q58034) was expressed in the *Escherichia coli* strain BL21(DE3)-RIL carrying the plasmid pETduet_MjFH$\alpha\beta$. Expression of the protein was induced with 0.3 mM isopropyl β- D-1-thiogalactopyranoside (IPTG) and grown for 18 h at 16 °C followed by lysis using a French press (Thermo IEC Inc.) at 1000 psi. The lysate was incubated at 70 °C for 30 min to precipitate the bacterial proteins followed by the addition of 0.01% polyethylenimine (PEI) to precipitate nucleic acids. The recombinant protein was purified using a Q Sepharose anion-exchange column, and the concentration was determined by the Bradford method[30] and stored at −80 °C as aliquots. A similar protocol was adopted for the purification of all of the mutants. Selenomethionine-incorporated MjFH$\alpha\beta$ was purified in a manner similar to that of the wild-type (WT). Growth conditions for cells expressing WT and selenomethionine-incorporated proteins and details of the protein purification protocol are provided in the Supporting Information.

Purified protein aliquots stored at −80 °C were reconstituted with an Fe−S cluster following standard protocols.[31,32] The protein solution was incubated in an anaerobic chamber (Coy) for 1 h to remove all traces of oxygen. All of the subsequent steps were performed under anaerobic conditions in the chamber. Briefly, around 10−50 μM protein was used for reconstitution. The reconstitution procedure was initiated by the addition of 50-fold excess dithiothreitol (DTT) to the protein solution followed by stirring for 30 min. Subsequently, 10-fold excess ferrous ammonium sulfate and sodium sulfide were added and stirred for another 3.5 h.

Interaction of MjFHα and MjFHβ Subunits. Interaction of the MjFHα subunit with the β-subunit was checked by incubating α-subunit-bound nickel Sepharose beads with an

https://doi.org/10.1021/acs.biochem.2c00541
Biochemistry 2023, 62, 476−493

excess of β-subunit at 26 °C for 30 min in buffer containing 20 mM Tris−HCl, pH 7.4. Following this, the beads were washed with the same buffer, and the α-subunit was eluted in the same buffer containing 500 mM imidazole. An aliquot of the eluate was loaded onto sodium dodecyl sulfate-polyacrylamide gel electrophoresis (SDS-PAGE) for separation and stained with Coomassie Brilliant Blue (CBB) for visualization. The oligomeric state of the copurified protein was probed by size exclusion chromatography on an analytical Superdex 200 10/300 GL column. Details of the buffer and standards used are provided in the Supporting Information.

The dissociation constant (K_d) of the MjFHα and β-subunit complex was estimated by isothermal calorimetry using a VP-isothermal titration calorimeter (MicroCal VP-ITC machine). For this purpose, 681 μM MjFHβ was taken in a syringe with 75 μM MjFHα and kept in the cell. In total, 30 injections of 10 μL each of MjFHβ were added to the sample cell containing MjFHα, and the cell contents were stirred at 300 rpm throughout the titration. The titration was performed at a constant temperature of 25 °C. Data were processed using Origin software, and the best fit model was used for K_d estimation.

Characterization of the Fe−S Cluster. A metal−thiolate charge transfer band was detected in the visible region using a 20 μM solution of the 4Fe−4S cluster reconstituted protein taken anaerobically in a 1 cm path length cuvette, sealed, and used for acquiring circular dichroism (CD) spectra in the region from 250 to 600 nm using a spectropolarimeter (Jasco J-810).

Enzyme Activity. All initial velocity measurements were conducted at 70 °C using a spectrophotometer (Hitachi U2010 spectrophotometer) placed outside the anaerobic chamber and initiated by the addition of the enzyme stored in the anaerobic chamber. The activity of MjFH was found to be maximal at pH 7.2, and hence all assays were carried out at this pH in 50 mM Tris−HCl. Conversion of fumarate to malate was measured spectrophotometrically as a decrease in absorbance caused by the depletion of fumarate. Details of the wavelengths and extinction coefficient values used are provided in the Supporting Information. Kinetics of inhibition by (*RS*)-2-thiomalate and details of the analysis of the initial velocity plots of WT and mutants are provided in the Supporting Information.

Crystallization and Data Collection. MjFHα, MjFHβ, and MjFH$\alpha\beta$ apo-protein, and MjFH$\alpha\beta$ holo-protein were set up for crystallization using the microbatch method.[33] Details of the methods adopted for setting up crystal trays are provided in the Supporting Information. Crystals of MjFHβ were obtained in 0.1 M bis-Tris, pH 5.5, and 25% poly(ethylene glycol) 3350 (PEG-3350). Crystals of MjFH$\alpha\beta$ apo-protein were obtained in 0.2 M magnesium chloride hexahydrate, 0.1 M bis-Tris, pH 5.5, and 25% w/v poly(ethylene glycol) 3350. Selenomethionine-incorporated MjFH$\alpha\beta$ (Se-MjFH$\alpha\beta$) also crystallized in the same condition, but crystals were not well formed. Well-formed crystals were obtained in the presence of an additive, nondetergent sulfobetaine (0.3 M NDSB-195) obtained from the Hampton additive screen. Crystals were cryo-protected by placing them for a brief period, in the initial condition with 20% (v/v) glycerol, before collecting diffraction data.

X-ray diffraction data on the MjFHβ protein crystal was collected on a Rigaku RU200 X-ray diffractometer equipped with a rotating anode-type light source with an osmic mirror that gives a monochromatic light source of wavelength 1.54179 Å. Selenium-single-wavelength anomalous dispersion (SAD) data were collected on Se-MjFH$\alpha\beta$ crystals at a wavelength of 0.9787 at the BM-14 beamline of the European Synchrotron Radiation Facility (ESRF).

Structure Determination and Refinement. The crystal structure of MjFHβ was solved by the molecular replacement method by making use of the *Archaeoglobus fulgidus* FH β-subunit (PDB ID: 2ISB) as the template for MR. The crystal structure of Se-MjFH$\alpha\beta$ was solved by selenium-SAD, making use of 11 anomalously scattering selenium atoms per functional dimer. Various packages available in the CCP4 suite[34] and Phenix modules[35] were used. Briefly, iMOSFLM[36] was used for data processing, SCALA[37] for data reduction and scaling, PHASER[38] for phasing in MjFHβ structure solution, and PHENIX AutoSol[35] for determining the position of selenium atom sites in Se-MjFH$\alpha\beta$. Automatic model building was performed for Se-MjFH$\alpha\beta$ using PHENIX AutoBuild.[39] REFMAC 5.0[40] and Phenix.refine[41] were used for refinement. Manual refinements were carried out using COOT.[42] Refinement statistics are summarized in Table S2. All of the structure-related figures were created using PyMol software.[43] Electrostatic surface potential was calculated using the Adaptive Poisson−Boltzmann Solver plugin in PyMol.[44]

Molecular Dynamics (MD) Simulations. Atomistic molecular dynamics simulations have been performed on five enzyme forms: (i) holo-LmFH (employing the crystal structure with PDB ID: 5L2R, refer to the Supporting Information and Figure S5 for more details), (ii) apo-LmFH (after removing the 4Fe−4S cluster and the substrate from the crystal structure of holo-LmFH), (iii) apo-MjFH (using the crystal structure obtained in this study), (iv) a model of holo-MjFH-1 (after docking the cluster and the substrate into the active site of apo-LmFH), and (v) a model of holo-MjFH-2 employing the contracted holo-MjFH structure obtained from a metadynamics simulation[45] (refer to the Supporting Information and Figures S8−S10 for more details). Simulations were carried out on the dimer forms of these enzymes at T = 300 K and P = 1 bar. The details on the simulation setup and simulation parameters are presented in the Supporting Information.

The CHARMM36m force field[46] was employed for the enzyme, whereas force field parameters for malate were generated using the CGenFF server.[47] Force field parameters for the 4Fe−4S cluster and the cysteine residues bound to it were taken from a previous report.[48] GROMACS-2018.3[49] was used for all of the MD simulations employing three-dimensional periodic boundary conditions. Refer to Table S6 for the number of atoms, cubic box length, and simulation lengths for the various simulated systems.

Quantum Chemical Calculations. All of the quantum chemical calculations were carried out using Gaussian 16 software.[50] Geometry optimizations were performed using the B3LYP functional along with the split valence Pople's type 6-31G(d,p) basis set[51−54] for all atoms except for Fe. For metals such as Fe, we chose the LANL2DZ basis set with an effective core potential (ECP).[55] Hessian calculations were carried out to characterize the stationary points as first-order saddle points, and the presence of a unique imaginary frequency was used to verify the transition states (TSs) for the small model systems. To further ascertain the correctness of the TS, intrinsic reaction coordinate (IRC) calculations were performed to identify the connecting reactant and product.[56−59] For all

https://doi.org/10.1021/acs.biochem.2c00541
Biochemistry 2023, 62, 476−493

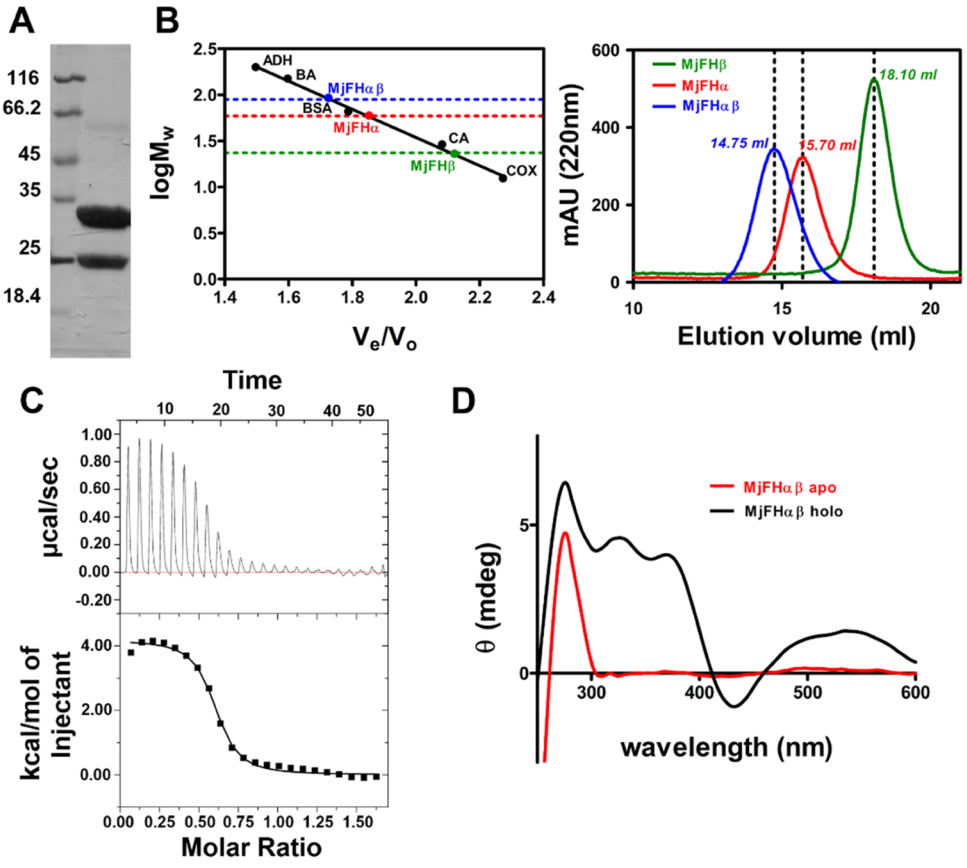

Figure 1. Purification and characterization of *M. jannaschii* fumarate hydratase. (A) α- and β-subunits associate in vitro. SDS-PAGE of 500 mM imidazole eluate from the Ni-NTA Sepharose matrix (lane 2). The $(His)_6$-tagged α-subunit of MjFH was bound to Ni-NTA Sepharose beads followed by incubation with the β-subunit and washing to remove the unbound protein. Thereafter, the protein bound to Ni-NTA beads was eluted with imidazole. Lane 1, molecular mass marker with molecular mass in kDa indicated to the left of the panel. (B) Size exclusion chromatograms (right panel) of α-, β-, and $\alpha\beta$-subunits of MjFH show that MjFH α is a constitutive dimer; MjFHβ a monomer, and MjFH$\alpha\beta$ a dimer of a heterodimer ($2\alpha + 2\beta$). The left panel shows a calibration plot of protein standards along with elution volumes of the peaks marked in the right panel. (C) Thermogram obtained by titration of MjFHα with MjFHβ in an isothermal calorimeter. (D) Visible circular dichroism spectra of apo-MjFH and Fe−S reconstituted holo-MjFH. The panel shows the characteristic dichroic pattern of the Fe−S cluster in holo-MjFH.

stationary points, single-point calculations were carried out using a higher basis set, 6-311+G** along with the D3 version of Grimme's dispersion correction.[60] To include the effect of the reaction medium, single-point calculations also included the solvent effect using Cramer and Truhlar's solvation model density (SMD) model[61] with water (ε = 80.4) as the solvent for small systems and diethyl ether (ε = 4.3) for the QM cluster approach.[62−67] In the QM cluster approach, quantum chemical methods, usually density functional theory (DFT), are used to treat a well-chosen region around the enzymatic active site, while the rest of the enzyme is approximated as a homogeneous polarizable medium. To avoid any conformational changes, the C_α atoms are frozen at their crystallographic positions. This might result in a few imaginary frequencies below 60 cm^{-1}, which do not affect the zero point energies (ZPE) much. The residues are typically truncated at C_α, and the truncated bonds are saturated by hydrogens. The ZPE, thermal, and entropic corrections calculated at 298.15 K and 1 atm pressure obtained in the gas phase at the B3LYP/6-31G(d,p)//6-31G(d,p),LANL2DZ(Fe) level of theory are added to the "bottom-of-the-well" energies obtained from the single-point energy calculations at the $SMD_{(water)}$/B3LYP/6-311+G** and $SMD_{(diethylether)}$/B3LYP/6-311+G**,LANL2DZ-(Fe) levels of theory. It should be noted that for the QM cluster approach, we only add the ZPE and thermal corrections, since entropy calculations with frozen atoms are unreliable. The entropic calculations require further extensive MD simulations, and as shown in an earlier work on cytidine deaminase by Åqvist and Himo, approaches like EVB (empirical valence bond approach) in conjunction with DFT can be used.[68] All of the energies discussed here are those obtained at the $SMD_{(water)}$/B3LYP/6-311+G**//B3LYP/6-31G(d,p),LANL2DZ(Fe) and $SMD_{(diethylether)}$/B3LYP/6-311+G**,LANL2DZ(Fe)//B3LYP/6-31G(d,p),LANL2DZ-(Fe) level of theory unless mentioned otherwise. For the QM cluster, natural population analysis (NPA) calculations were further carried out at the $SMD_{(diethylether)}$/B3LYP/6-311+G**,LANL2DZ(Fe) level of theory using the gas-phase optimized geometries at the B3LYP/6-31G(d,p),LANL2DZ-(Fe) level of theory. (See the Supporting Information for full computational details.)

RESULTS

Structure of MjFH. MjFHα and MjFHβ subunits when coexpressed in *E. coli* coelute upon purification by ion-exchange chromatography on a Q Sepharose column. Pull down of MjFHβ using MjFHα as bait on Ni-NTA Sepharose beads confirmed the formation of a protein complex (Figure 1A). Analytical size exclusion chromatography of MjFHα,

https://doi.org/10.1021/acs.biochem.2c00541
Biochemistry 2023, 62, 476−493

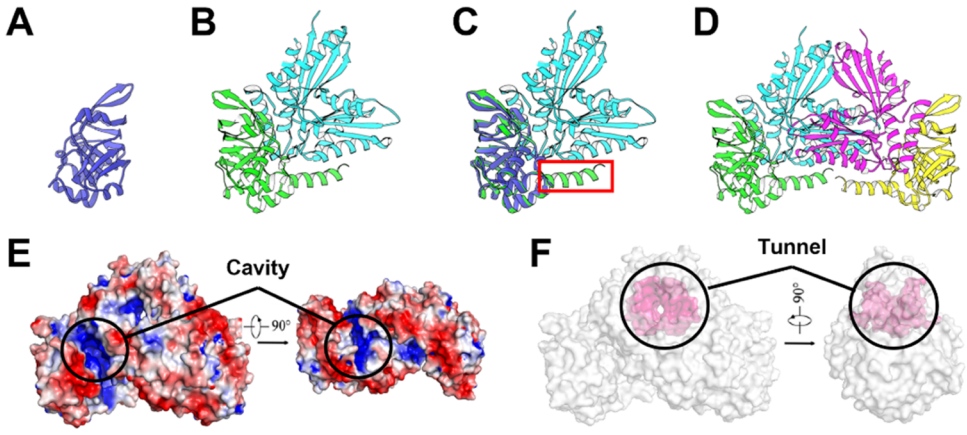

Figure 2. Structure of MjFH. (A, B, D) Structure of the MjFHβ monomer, the MjFH$\alpha\beta$ heterodimer, and the MjFH$\alpha\beta$ biological assembly of the tetramer. α-Subunits are in cyan and magenta color, while β-subunits are in green and yellow color for the complex and dark blue for the MjFHβ structure. (C) Overlay of the MjFHβ monomer on the MjFH$\alpha\beta$ dimer reveals the ordering of the C-terminal α-helix (enclosed in a red box) in the β-subunit of the MjFH$\alpha\beta$ complex, which is disordered in the MjFHβ structure. (E) Surface electrostatic potential of the MjFH$\alpha\beta$ tetramer. A positively charged cavity is located between the interface of α- and β-subunits creating the active site pocket. (F) Protein tunnel. Highlighted in pink is a tunnel that is formed between the α-subunits of MjFH that passes through the entire breadth of the protein.

MjFHβ, and MjFH ($\alpha\beta$ complex) showed molecular masses of 60, 22, and 93 kDa corresponding to a homodimer, a monomer, and a heterotetramer of 2α- and 2β-subunits, respectively (theoretical mass of α = 33 kDa, β = 22 kDa) (Figure 1B). The 2α−2β-subunit stoichiometry of the complex was further verified through isothermal calorimetry, where the resultant thermogram (Figure 1C) fitted best to the one-site binding model, and the K_d value of 595 ± 19 nM indicated tight interaction between the α- and β-subunits. Visible CD, sensitive to changes in the Fe−S cluster environment in proteins,[69] did not show any circular dichroic effect in the visible region for the unreconstituted, apo-protein, while the 4Fe−4S reconstituted MjFH$\alpha\beta$ showed a characteristic spectrum in the visible region (Figure 1D).

Attempts were made to crystallize individual subunits of MjFH and the complex in both apo- and holo-protein states. In all conditions attempted, only the MjFHβ and MjFH$\alpha\beta$ apo-protein complex crystallized. The MjFHβ subunit structure was solved by molecular replacement using the β-subunit structure of *A. fulgidus* (PDB ID: 2ISB) and refined to a resolution of 2.3 Å (Table S2). The structure of the MjFH$\alpha\beta$ apo-protein complex was solved by single-wavelength anomalous dispersion (SAD) using crystals of the selenium-incorporated protein and refined to 2.45 Å resolution (Table S2). MjFHβ forms a crystallographic dimer that does not have any physiological relevance, as analytical size exclusion chromatography shows only monomers in solution. The asymmetric unit in the MjFH$\alpha\beta$ complex contains one copy each of α- and β-subunits, and the functional form of the enzyme, which is a dimer of a heterodimer (Figure 2A,B), was generated using a symmetry-related mate from the neighboring unit cell (Figure 2D). The MjFHβ structure overlays well on the β-subunit of the MjFH$\alpha\beta$ apo-protein complex with an root-mean-square deviation (RMSD) of 0.528 Å. A 14-residue stretch at the C-terminal end of the protein that was disordered in the MjFHβ structure ordered into an α-helix in the MjFH$\alpha\beta$ complex (Figure 2C). Ordering of the 14-residue α-helical stretch is aided by a helix−helix interaction with the α-subunit (Figure S1). This 14-residue helical stretch is absent in the class-I single-subunit *L. major* FH (LmFH) and may enable tight binding of the two subunits. The LmFH structure is shown to have a previously unidentified $\alpha + \beta$ fold and searching MjFHα in the DALI server to identify the fold, picked the LmFH structure as the strongest match with an RMSD of 2.1 Å (PDB ID: 5L2R). The SCOP database[70] classifies the fold of MjFHβ as "swiveling $\beta/\beta/\alpha$" similar to the CTD in LmFH, which is considered to be a highly mobile segment in multidomain proteins. The surface electrostatic potential of MjFH reveals a large positively charged active site cavity between the α- and β-subunits of MjFH akin to that between NTD and CTD of LmFH (Figure 2E). A tunnel originating from a cavity at the top of the protein, observed in LmFH as well, passes through the entire breadth of the protein without connecting to the active site cavity (Figure 2F).

Differences between Class-I Apo- and Holo-FH. To understand structural similarities and differences between MjFH and LmFH, the structures of the two proteins were superposed. Although the MjFHα and β-subunits individually superpose well with the N-terminal and C-terminal domains of LmFH with RMSDs of 1.8 and 1.4 Å, respectively (Figure 3A,B), the structural superposition of the biological assemblies of the two proteins showed gross differences with an RMSD of 4.95 Å (PDB ID: 5L2R; Figure 3C). A visual inspection revealed that the LmFH structure is more compact than the MjFH structure, and measuring the distance between conserved residues located at the extreme termini of both proteins showed that the α-subunits and N-terminal domains of MjFH and LmFH are equidistant, while the β-subunits in MjFH are spaced farther apart than the C-terminal domains of LmFH (Figure 3D). In LmFH, the CTD has been shown to be mobile and its mobility changes with substrate/inhibitor binding. The *B*-factor values for the swiveling β-subunit, as expected, is higher than that of the α-subunit of the protein (Figure 3E). A major proportion of residues at the NTD/NTD or α/α dimer interface of class-I FH is found to be conserved,[27] and an interface analysis reveals that LmFH has a larger number of interactions between the domains of the protein, possibly accounting for its compact structure. While the NTD/NTD interface in LmFH is stabilized by 42 hydrogen bonds with an overall interface interaction area of 3712 Å^2, the α/α-subunit interface in MjFH is stabilized by 34 hydrogen bonds with an interface interaction area of 2521 Å^2.

https://doi.org/10.1021/acs.biochem.2c00541
Biochemistry 2023, 62, 476−493

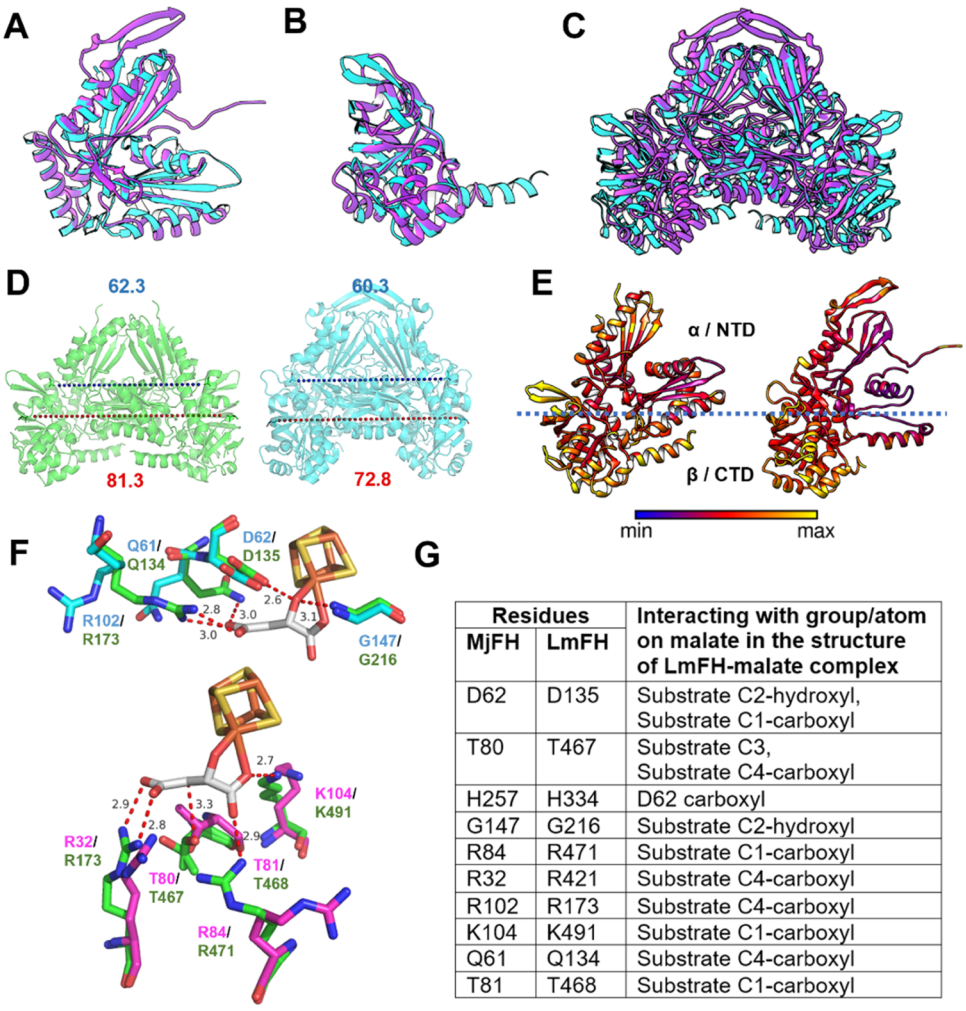

Residues		Interacting with group/atom on malate in the structure of LmFH-malate complex
MjFH	LmFH	
D62	D135	Substrate C2-hydroxyl, Substrate C1-carboxyl
T80	T467	Substrate C3, Substrate C4-carboxyl
H257	H334	D62 carboxyl
G147	G216	Substrate C2-hydroxyl
R84	R471	Substrate C1-carboxyl
R32	R421	Substrate C4-carboxyl
R102	R173	Substrate C4-carboxyl
K104	K491	Substrate C1-carboxyl
Q61	Q134	Substrate C4-carboxyl
T81	T468	Substrate C1-carboxyl

Figure 3. Differences between apo-MjFH and holo-LmFH (5L2R) structures. Superposition of LmFH NTD on MjFHα (A) and LmFH CTD on MjFHβ (B) shows good alignment with RMSD values of 1.8 and 1.4 Å, respectively. (C) Overlay of the LmFH functional complex on MjFH shows gross structural differences and a lack of clear alignment, with an RMSD of 4.95 Å. (D) Distance between conserved residues Ala52 and Ala125 located at the extreme ends of MjFHα (green) and LmFH NTD (blue) dimers show similar spacing, while the distance between conserved residues Val160 and Val546 of MjFHβ and LmFH CTD shows that the β-subunits of MjFH are more distantly spaced than the CTD of LmFH. (E) *B*-factor analysis reveals that MjFHβ and LmFH CTD have higher B-factor values than the overall average of the protein. (F) Active site residues in MjFH compared to LmFH. The upper panel shows the superposition of active site residues from MjFHα (blue) on LmFH NTD (green) and the lower panel shows the superposition of active site residues from MjFHβ (magenta) on LmFH CTD (green). Malate bound to the cluster is highlighted in gray. Residues Gln61 and Arg102 from the α-subunit and Arg84 from the β-subunit of MjFH show different side-chain rotameric conformations. Numbers adjacent to the dashed lines are distances in Å. Of the two residue numbers given, the upper is for MjFH and the lower for LmFH. (G) Numbering of the active site residues of MjFH and LmFH. Note that the contacts with the atoms on the substrate are from the LmFH structure.

Similarly, 19 hydrogen bonds stabilize the NTD−CTD domains of LmFH with an interface area of 1503 Å^2, while only five hydrogen bonds are observed between the α- and β-subunits of MjFH with an interface area of 1275 Å^2. Five residues are involved in van der Waals interactions between the CTDs of LmFH but the β-subunits of MjFH do not form any contacts (Table S3).

Transposing the Fe−S cluster from LmFH onto MjFH reveals that three cysteine residues, Cys60, Cys182, and Cys269, in MjFH are well positioned to bind to the cluster (Figure S2). The LmFH active site has nine residues present in loops, hydrogen bonding with the substrate at the active site (residue numberings of all nine residues for both MjFH and LmFH are provided in Figure 3G). All nine active site residues are well conserved across both class-I single-subunit and two-subunit-type FHs (Figure S3). Six of these residues are positioned similarly in the MjFH apo-protein active site, while three other residues (Gln61 and Arg102 from the α-subunit and Arg84 from the β-subunit) adopt a different side-chain rotameric conformation to show that the active site is largely preorganized even in the absence of the cluster and the substrate (Figure 3F).

Binding of the Cluster and Substrate Compact Quaternary Structure. The inter-CTD distance (the distance between the centers of mass (COM) of the CTDs (LmFH)/β-subunits (MjFH)) and the radius of gyration (R_g) in the crystal structure of apo-MjFH are greater than those of holo-LmFH (Table S7), as can also be visually inferred from the overlay of the two structures (Figure 3C). To identify the molecular determinants for this difference, atomistic molecular dynamics simulations were carried out on both apo- and holo-forms of both MjFH and LmFH (see the "Computational Details" section in the Supporting Information). Force field parameters employed herein were validated by examining the

https://doi.org/10.1021/acs.biochem.2c00541
Biochemistry 2023, 62, 476−493

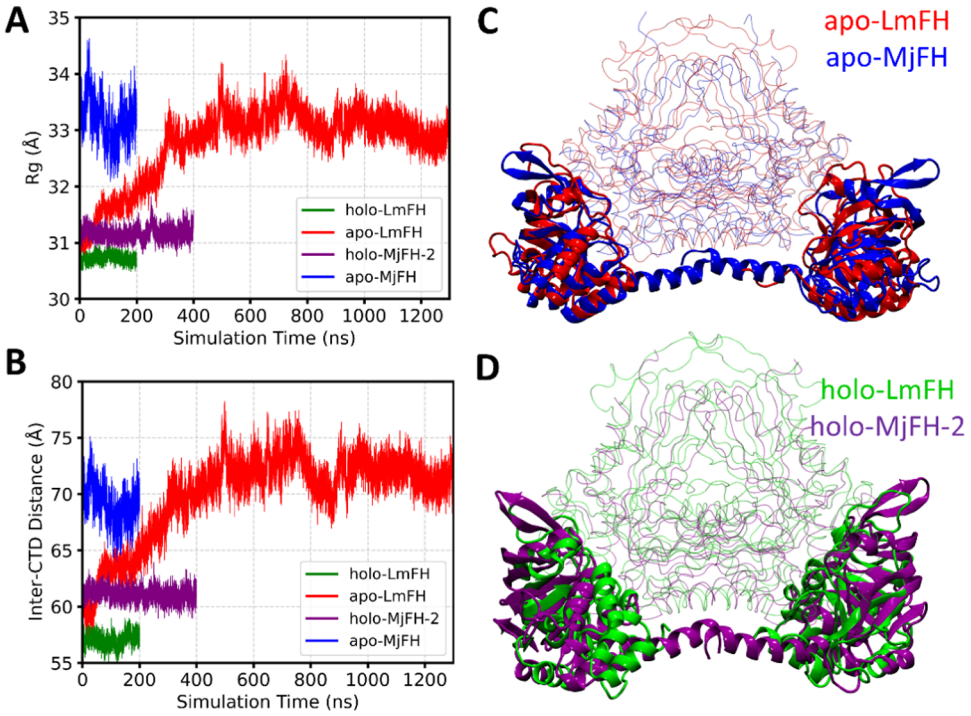

Figure 4. MD simulations reveal that class-I FH adopts two different states based on either the presence or absence of a bound 4Fe−4S cluster and the substrate. (A) R_g and (B) inter-CTD distance as a function of simulation time for holo-LmFH (green), apo-LmFH (red), holo-MjFH-2 (purple), and apo-MjFH (blue). Refer to Figure S7 for the same for the holo-MjFH-1 model. Apo-LmFH expands relative to holo-LmFH, and both the R_g and inter-CTD distance values increase initially and remain saturated for the last 300 ns of simulations. (C) Overlay of the representative structure of apo-LmFH with that of apo-MjFH. (D) Overlay of the representative structure of holo-MjFH-2 with that of holo-LmFH. The representative structures are obtained using cluster analysis on the last 100 ns of simulations. The CTDs (LmFH)/β-subunits (MjFH) are shown in the cartoon representation, whereas the remaining parts of the enzymes are shown in transparent lines. The R_g for LmFH is calculated excluding the highly flexible 63-residue long modeled fragment, and this peptide fragment is not shown in the overlay panels (C, D).

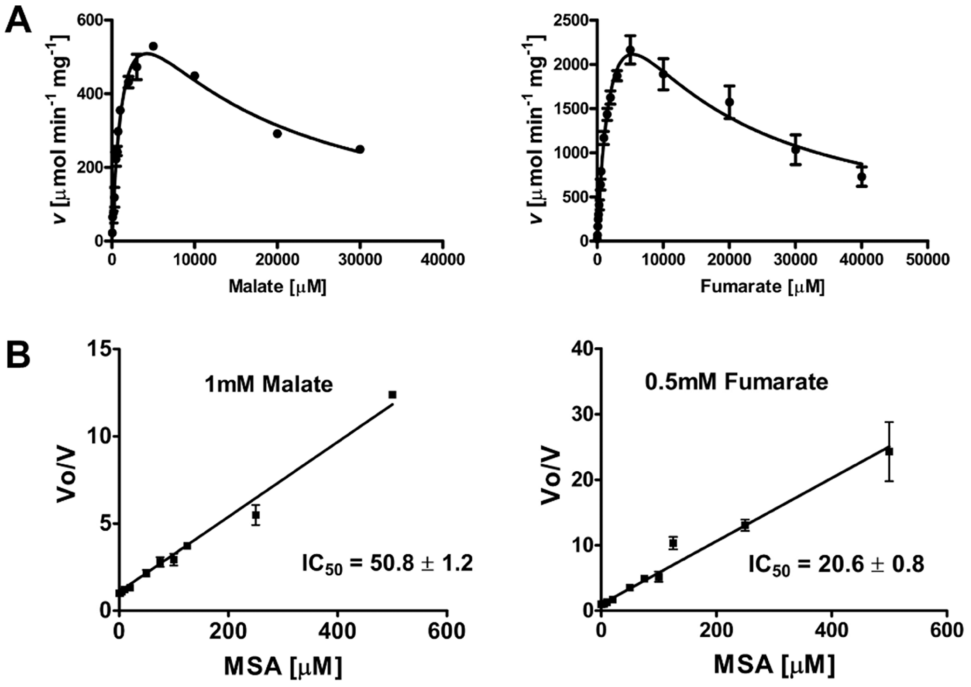

Figure 5. MjFH kinetics and IC_{50} plot for inhibition by (*RS*)-2-thiomalate. (A) Initial velocity as a function of substrate concentration for malate (left panel) and fumarate (right panel). Data were fit to the substrate inhibition equation (eq 1 in the Supporting Information). (B) IC_{50} plot for (*RS*)-2-thiomalate with malate (left panel) and fumarate (right panel) as substrates. The unit for IC_{50} values is μM.

stability of holo-LmFH, the cluster, and the substrate during the course of the simulation (Figure S6A). A visual inspection of the structure of the 4Fe−4S cluster and the bound malate at a 200 ns simulation time frame of holo-LmFH (Figure S6B)

https://doi.org/10.1021/acs.biochem.2c00541
Biochemistry 2023, 62, 476−493

also illustrates that the malate and the cluster are intact and stable. Next, we created a model for holo-MjFH by docking the cluster and the substrate into the experimentally determined apo-MjFH structure (see Tables S4 and S5 and Figure S11 in the Supporting Information for docking details). This simulation, hereinafter referred to as holo-MjFH-1, however, did not result in the contraction of the holo-MjFH enzyme (Figure S7). Thus, we resorted to metadynamics[45]-based MD simulations to arrive at a model structure for holo-MjFH, and these simulations, hereafter referred to as holo-MjFH-2, (see the "Metadynamics Simulation of Holo-MjFH to Obtain a Contracted Structure" subsection in the Supporting Information for details) indeed resulted in a stable structure, contracted with respect to the apo-MjFH enzyme. Both the inter-CTD distance and R_g values of holo-MjFH-2 stay stable during the entire course of the simulation (Figure 4A,B). An increase in the inter-CTD distance and R_g values in the simulation of apo-LmFH as well strongly suggests that the class-I FH structure contracts or expands based on the presence or absence of the bound Fe−S cluster and the substrate. Both these values for apo-LmFH increase initially and reach a plateau after 800 ns of simulations (Figure 4B). Structures of all of the enzyme forms obtained as that representing the major cluster (obtained using the GROMACS cluster module) over the last 100 ns of the corresponding trajectories are overlaid and presented in Figure 4C,D. The cartoon representations show that the CTDs of both the apo (expanded) and holo (contracted) forms of MjFH superpose better with the corresponding forms of LmFH than the alignment of apo-FH (expanded) on holo-FH (contracted) (Figures 3C and S12A,B). The superposition of apo-LmFH on holo-LmFH (Figure S12C) and apo-MjFH on holo-MjFH (Figure S12D) clearly demonstrates that the movement of the CTD/β-subunit is responsible for the expansion of the apo-form of class-I FH.

Kinetics and Site-Directed Mutagenesis. The activity of the purified recombinant enzyme was measured at 240 nm as a time-dependent increase or decrease in the absorbance of fumarate in the assay mixture. The MjFH apo-protein, β-subunit, and reconstituted α-subunit were found to be inactive, while addition of MjFHβ to Fe−S reconstituted MjFHα yielded high levels of activity. The kinetic parameters of MjFH for activity on malate and fumarate were obtained by fitting v versus [S] plots to the substrate inhibition equation (eq 1 in the Supporting Information and Figure 5A). K_M, K_I, and V_{max} values derived from the fits are summarized in Table 1. The catalytic efficiency (k_{cat}/K_M) of MjFH for both malate and fumarate is comparable to other reported class-I FHs. (*RS*)-2-Thiomalate was found to inhibit MjFH with IC_{50} values of 50.8 ± 1.2 and 20.6 ± 0.8 μM with malate and fumarate as substrates, respectively (Figure 5B). The values of the apparent inhibitory constant K_I (app) for (*RS*)-2-thiomalate derived from the IC_{50} values with malate and fumarate as substrates were 30.8 and 17.4 μM, respectively, similar to those previously reported for class-I FHs.[10,25,71]

To understand the catalytic mechanism of class-I FHs, residues were selected for site-directed mutagenesis in MjFH, which according to the (*S*)-malate-bound *L. major* FH (5L2R) structure and more recently solved inhibitor—thiomalate-bound structure (6MSO, 6MSN) can interact with the substrate. A set of 10 residues are located at the active site of which 9 are in hydrogen-bonding distance with (*S*)-malate (Gln61, Asp62, Arg102, Gly147 from the α-subunit and Arg32,

Table 1. Kinetic Parameters of MjFH WT and Mutant Enzymes

MjFH mutants	corresponding residues in LmFH	malate				fumarate			
		V_{max} (μmol min^{-1} mg^{-1})	K_M (μM)	K_I[a] (μM)	k_{cat}/K_m ($s^{-1}M^{-1}$)	fold change in catalytic efficiency	V_{max} (μmol min^{-1} mg^{-1})	K_M (μM)	K_I[a] (μM)	k_{cat}/K_m ($s^{-1}M^{-1}$)	fold change in catalytic efficiency
WT	-	**883 ± 55**	**1554 ± 169**	**11539 ± 1466**	**5.1 x 10^5**	-	**4309 ± 384**	**2785 ± 397**	**10320 ± 1548**	**1.4 x 10^6**	-
D62V	D135	15.7 ± 2.1	1030 ± 238	13750 ± 4377	1.37 x 10^4	37.2	45.3 ± 4.9	808 ± 154	8839 ± 1951	5 x 10^4	28
T80V	T467	4.7 ± 0.8	1632 ± 389	6453 ± 1840	2.6 x 10^3	196.1	11.3 ± 1.5	1713 ± 324	4151 ± 858	6 x 10^3	234.5
T80C	T467	Inactive									
H257N	H334	11.8 ± 0.9	590 ± 86	12247 ± 2157	1.8 x 10^4	28.3	118 ± 13	3343 ± 559	11451 ± 2401	3.2 x 10^4	43.8
D62V+H257N	D135+H334	Inactive									
G147A	G216	Inactive									
K144L	K213	6.5 ± 0.3	446 ± 51	35077 ± 7308	1.3 x 10^4	39.2	17.2 ± 0.9	557 ± 72	24571 ± 4843	2.8 x 10^4	50
S148A	S217	333 ± 30	680 ± 122	21790 ± 5099	4.4 x 10^5	1.1	1286 ± 275	1755 ± 517	4605 ± 1531	6.6 x 10^5	2.2
R84K	R471	34.5 ± 2.8	749 ± 110	10986 ± 1958	4.1 x 10^4	12.4	108.6 ± 6.5	1063 ± 125	19872 ± 3426	9.2 x 10^4	14.2
R32K[b]	R421	S.A. at 1mM malate		0.46 ± 0.06			S.A. at 500 μM fumarate		1.36 ± 0.23		
R102K[b]	R173			1.12 ± 0.10					0.30 ± 0.02		
K104L[b]	K491			0.825 ± 0.001					0.94 ± 0.03		
Q61L	Q134	Inactive									
T81V	T468	Inactive									
R32L	R421	Inactive									
R84L	R471	Inactive									
R102L	R173	Inactive									

[a]KI values provided in the table refer to the inhibitory constants arising from the inhibition of the enzyme by the substrate. [b]Since these mutants were weakly active, only specific activity (S.A.) values are reported at the indicated substrate concentration.

https://doi.org/10.1021/acs.biochem.2c00541
Biochemistry 2023, 62, 476−493

Thr80, Thr81, Arg84, and Lys104 from the β-subunit; Figure 3G). The residue/s closest to the C3 carbon of (*S*)-malate is Thr80 at 3.34 Å and to the C2 hydroxyl group are Asp62 and Gly147 at 2.64 and 3.1 Å distance, respectively. Another residue His257 from the α-subunit, although not interacting with the substrate, is hydrogen-bonded to Asp62 at a distance of 2.81 Å and could stabilize the charge state of this residue. All other residues form H-bonds with the carboxyl groups of (*S*)-malate. Sequence alignment also shows that Gly147 is part of the "KGXGS" motif that is highly conserved in class-I FH (Figure S3), and considering their proximity to the substrate, Lys144 and Ser148 from the motif were also chosen for mutation.

To examine the function of the 10 active site residues and 2 conserved residues from the KGXGS motif, all these 12 residues were replaced by site-directed mutagenesis. Mutant enzymes were generated and purified using protocols similar to the WT protein. Steady-state kinetics were conducted under conditions similar to those used for WT, and the kinetic parameters along with the fold change in catalytic efficiency relative to WT are summarized in Table 1. Mutants with measurable activities showed a small decrease in the K_M value, between 1.5- and 3-fold for both substrates, which is close to that observed in LmFH mutants. The K144L mutant where K144 is part of the KGXGS motif had the highest decrease in K_M values by 3.5- and 5-fold, respectively, for malate and fumarate, suggesting a possible role in substrate binding. Unlike in LmFH where mutation of residues corresponding to threonine80 and aspartate62, the proposed catalytic base and acid, respectively, led to a large decrease (2500−5500-fold) in catalytic efficiency, MjFH_T80V and MjFH_D62V retained significant activity. The mutant T80V of MjFH showed a 196- and 235-fold decrease in catalytic efficiency for malate and fumarate, respectively, while MjFH_D62V showed a 37- and 28-fold reduction for the two substrates, respectively. Mutation of threonine to cysteine, however, led to MjFH_T80C being inactive. A similar trend has been observed in adenylosuccinate lyase, where mutating the serine residue believed to be the catalytic base to alanine led to a 1000-fold decrease in specific activity while mutating it to cysteine abolished activity. It is suspected that the highly reactive thiol group of cysteine disrupts the active site by geometric and electrostatic perturbations.[72] Mutation of the histidine residue in contact with the predicted catalytic acid to asparagine in MjFH_H257N also led to a 28- and 44-fold reduction in catalytic efficiency for both substrates. A double mutant of D62V and H257N of MjFH was inactive, suggesting the requirement of at least one of these residues at the active site. While the mutant K144L from the KGXGS motif showed a decrease in catalytic efficiency of 39- and 50-fold for malate and fumarate as substrates, S148A showed no decrease in catalytic efficiency for malate and a 2-fold decrease for fumarate as the substrate. Mutation of Gly147 of the KGXGS motif to alanine led to an inactive enzyme. The backbone amide NH of G147 is at 3.1 Å from the C2 hydroxyl group of malate in the malate-bound structure of LmFH and mutating it to alanine could lead to the side chain occupying the active site space, resulting in short contacts that occlude substrate binding.

Mutation of all other residues (Gln61, Arg102, Gly147, Arg32, Thr81, and Arg84) at the active site, which are in close contact with the carboxyl groups of the substrate, to a residue with a nonpolar side chain led to inactive mutants except for the mutant MjFH_K104L that exhibited very feeble activity, precluding estimation of K_M and V_{max} values. Lys and Arg were mutated to leucine to retain as close as possible the volume occupied by the side chains of the residues and to avoid the formation of a cavity at the active site. It must be noted that the corresponding mutants (R173A, R421A, and R471A) in LmFH exhibited weak activity.[73] Our inability to detect this weak activity could be due to the differences in oxygen levels across the two experimental setups: 0.1 versus 6 ppm.

A cluster of positively charged residues is arrayed around the dicarboxylate substrate, thereby polarizing the reactive carbon−carbon double bond. Two arginine residues and one glutamine (Arg32, Arg102, and Gln61) clamp the substrate from one side (side A, Figure 6) and one lysine, arginine, and

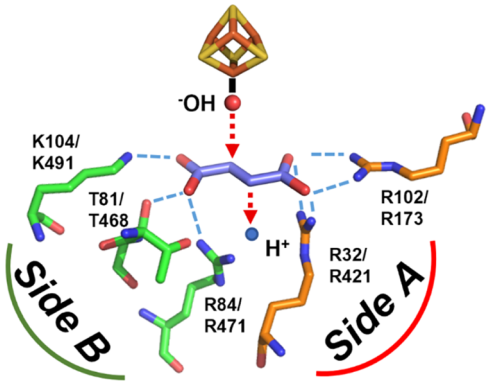

Figure 6. Substrate is charge-polarized at the active site with more charge interactions on one side than those on the other. Residues Arg102 and Arg32 on side A form four strong hydrogen bonds with the carboxyl group of the bound substrate compared to one bond each formed by Lys104 and Arg84 on side B. Dashed lines indicate hydrogen bonds. Of the two residue numbers given, the upper is for MjFH and the lower for LmFH.

threonine residue (Lys104, Arg84, and Thr81) clamp from the other side (side B, Figure 6). The positively charged residues are asymmetrically distributed about the symmetric substrate facilitating charge polarization. The hydrogen-bonding network on side A is mediated by four strong bonds formed by two arginine residues (Arg32 and Arg102), in contrast to side B, which has only two hydrogen bonds from one lysine and one arginine residue (Lys104 and Arg84).

As the charged side chains of these residues could essentially have a role in catalysis by polarizing the substrate and priming it for the reaction, the three arginine residues were mutated to lysine, and the mutants probed for activity. Both the arginine residues on side A, which form stronger hydrogen bonds with the substrate, on mutating to lysine (R32K and R102K) retained feeble activity, precluding estimation of kinetic parameters, while mutating the arginine on side B to lysine (R84K) led to a 10-fold decrease in catalytic efficiency for both substrates (Table 1). Mutating the charged residues on side A was more detrimental than that on side B. All inactive mutants showed a characteristic CD spectrum in the near-UV/visible region, confirming that Fe−S cluster assembly is intact in these mutants (Figure S4).

Fumarate Hydration in Aqueous Solution Proceeds through the Carbanion Intermediate. Although in aqueous medium, the thermodynamics for malate (**A**)-to-fumarate (**C**) conversion has been worked out,[4] the reaction mechanism has not been fully explored. A general mechanism

https://doi.org/10.1021/acs.biochem.2c00541
Biochemistry 2023, 62, 476−493

for interconversion between fumarate and malate involving a carbanion intermediate (Scheme 2) has been proposed, and

Scheme 2. Three Pathways of Interconversion between Malate and Fumarate in Aqueous Medium[a]

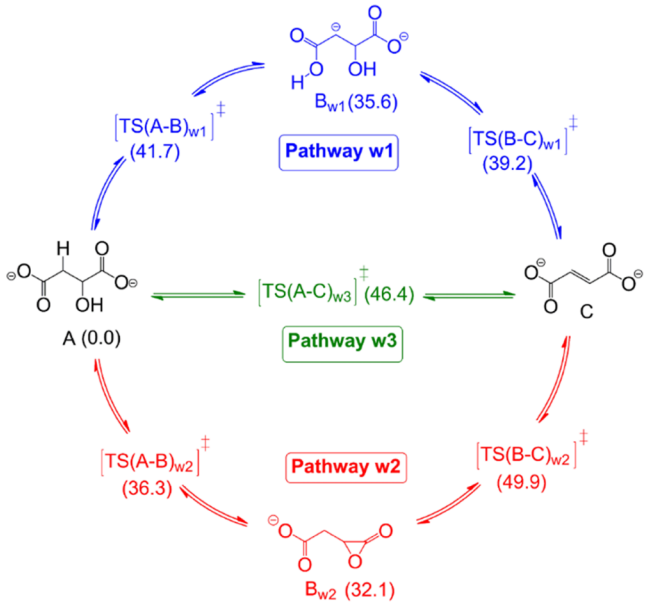

[a]Values in parentheses are the relative electronic energies in kcal mol^{-1}. The energy shown for **TS(A−C)$_{w3}$** involves an external water molecule, and concerted TS with no external water molecule is found to be even higher in energy (details are provided in Scheme S1 and Figure S14 in the Supporting Information).

this merits a fresh examination to enable comparison with that of the enzyme-catalyzed reaction. Hence, the first calculations were to understand/elucidate the mechanism in aqueous medium. Three different mechanisms, pathway w1 involving a carbanion, pathway w2 involving a carbocation, and pathway w3 involving a concerted TS (transition-state), have been studied. In pathway w1, the first step of malate to fumarate conversion involves proton abstraction by a water molecule via **TS(A−B)$_{w1}$**, as shown in Figure 7. The second step involves

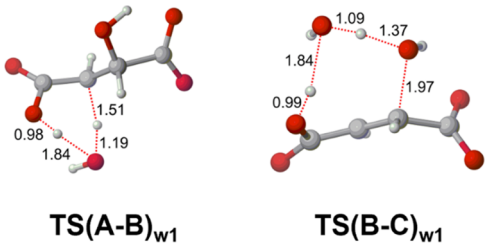

Figure 7. Optimized geometry of the two transition states of the nucleophilic pathway (w1) in aqueous medium. Distances are in Å.

the removal of a water molecule via **TS(B−C)$_{w1}$**. In pathway w2, the first step involves water removal as shown in **TS(A−B)$_{w2}$**, whereas the second step involves proton abstraction via **TS(B−C)$_{w2}$** (Scheme S1 and Figure S13) as opposed to pathway w1. For pathway w3, the conversion happens through a single TS of water removal (refer to Scheme S1 for more details). The optimized geometries for TSs involved in the carbocation pathway (w2) and the concerted pathway (w3) can be seen in Figure S13. As seen from the relative energies provided in parentheses in Scheme 2, the carbanion pathway, i.e., pathway w1, is found to be of the lowest energy. It presents an activation energy barrier of 41.7 kcal mol^{-1}, which is in accordance with the experimental value of 36 kcal mol^{-1}. The optimized geometries for TSs involved in the carbanion pathway are shown in Figure 7. In the first **TS(A−B)$_{w1}$**, the water molecule abstracts the proton from the C3 carbon and relays it to the carboxylate group via a six-membered TS. In the second **TS(B−C)$_{w1}$**, the C−O bond cleaves where a water molecule donates a proton to the departing OH^- and simultaneously abstracts the proton from the carboxylate ion, thereby generating fumarate.

Reaction Mechanism at the Enzyme Active Site. To understand the transition-state stabilization brought out by the enzyme, which corresponds to an enormous catalytic rate enhancement (~3.5 × 10^{15}-fold at pH 6.8 and 37 °C) compared to the uncatalyzed reaction, the QM cluster method was utilized to probe into the reaction mechanism. Two different QM cluster models (Figure 8) were built for this study from the available X-ray crystal structure of FH from *L. major* (PDB ID: 5L2R). In the smaller QM cluster (QM1) consisting of 86 atoms, only five essential amino acid residues (Asp135, His334, Thr467, Thr468, and Arg471), which are believed to play an active role in the catalytic cycle, were included. On the other hand, in the larger QM cluster (QM2), consisting of 207 atoms, 13 amino acid residues along with the 4Fe−4S cluster were considered. Out of these 13 residues, three cysteine residues (Cys133, Cys252, and Cys346) are bound to three Fe atoms in the 4Fe−4S cluster. Leaving the catalytic residues aside, five additional amino acid residues that interacted noncovalently with the bound substrate via hydrogen bonding (Gln134, Arg173, Gly216, Arg421, and Lys491) were included in QM2. Apart from the residues, a crystal water molecule was also included in QM2. Akin to the aqueous medium, here also we investigated three possible mechanistic pathways of interconversion using the QM1 model (refer to Schemes S2 and S3 and Figure S15 in the Supporting Information). The conventional pathway of olefinic hydration did not seem to be operational even inside the enzymatic active site with a high activation barrier of 42.8 kcal mol^{-1} (Figure S16). Although the carbanion pathway turned out to be the most favorable in this case as well, the energy barrier obtained was 21.2 kcal mol^{-1} with the QM1 model, which is higher than the experimentally known value of 13.8 kcal mol^{-1}.[4] However, the energy barrier reduced significantly to 16.7 kcal mol^{-1} in the larger QM2 model, signifying the importance of noncovalent interactions present at the active site. In the optimized geometry of the QM2 model, as shown in Figure 8, the catalytic base Thr467 and the catalytic acid Asp135 are suitably placed, maintaining the H-bonding contacts as seen in the crystal structure. In **TS(A−B)$_{wt}$**, Thr467 abstracts a proton from the substrate and simultaneously donates its proton to the neighboring Arg471, resulting in the formation of the carbanion (Figure 9). In the second **TS(B−C)$_{wt}$**, OH^- dissociates from the carbanion and at the same time accepts a proton from Asp135, thereby generating fumarate with the release of a water molecule.

Alternative Mechanism in the Absence of Catalytic Residues. To evaluate the effect of the mutation of catalytic residues on the reaction mechanism, we used the QM2 model and generated two mutants Thr467A (M1) and Asp135A (M2). In M1, the Thr467 residue is mutated to alanine, which cannot relay proton transfer. The obvious choice for an

https://doi.org/10.1021/acs.biochem.2c00541
Biochemistry 2023, 62, 476−493

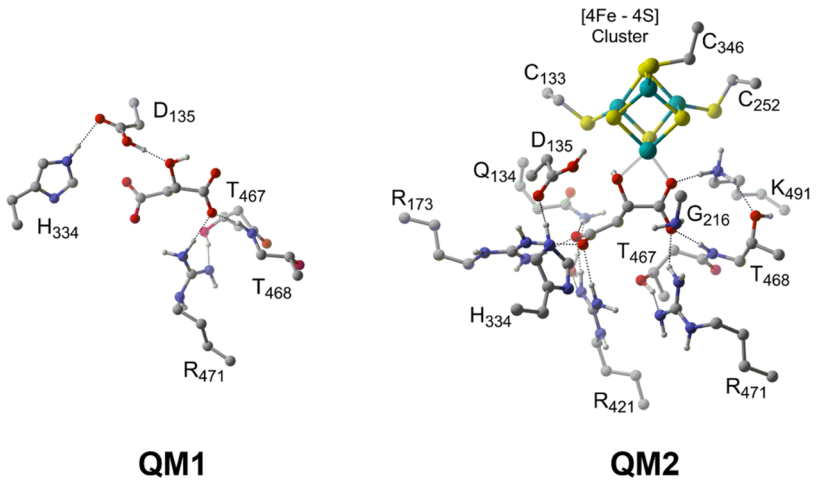

Figure 8. Optimized geometries of malate-bound smaller (QM1) and larger (QM2) QM cluster models.

alternate base is the crystal water, which can assist the proton transfer from C3 of malate to Arg471 as shown in $\mathbf{TS(A-B)}_{M1}$. In the second $\mathbf{TS(B-C)}_{M1}$, the Asp135 residue plays a similar role as that in the wt. In the second mutant Asp135A (M2), where the catalytic acid Asp135 was mutated to alanine, the second **TS(B−C)** could not be optimized with crystal water, as free OH^- is not as stable as the negatively charged aspartate residue. We, therefore, considered an alternative possibility where the His334 residue exists in its protonated form (H334-H^+). It can then transfer a proton through the water molecule to the departing OH^-, eventually eliminating a water molecule from the carbanion via $\mathbf{TS(B-C)}_{M2}$ (Scheme S4). The activation energy barriers for M1 and M2 were found to be 26.4 and 23.2 kcal mol^{-1}, respectively (Figure 11). While these barriers are higher than the experimentally observed values, our model qualitatively captures the increase in activation energies in these mutants.

DISCUSSION

In this study, through mutational analysis and DFT calculations, we propose a mechanism for the rate enhancement displayed by class-I FHs. We also see features distinct in MjFH.

MjFH Structure and Catalysis. The two subunits of MjFH remain tightly associated even in the absence of the ligand or Fe−S cluster. The α-subunit is inactive and requires the association of the β-subunit for activity. The structure of MjFH solved is the first structure of a two-subunit class-I FH. At the time of solving the MjFH apo-protein structure, the LmFH structure was not available, and SAD phasing was carried out to solve the structure of the $\alpha\beta$-complex. The two FH structures are indicative of two different states of the protein, a slightly relaxed MjFH apo-protein state and a more compact LmFH holo-protein state. The primary difference is in the β-subunit and the CTD of the proteins, which are spaced differently. MD simulations carried out with the apo- and holo-structures of LmFH and MjFH show that the enzyme expands upon the removal of the Fe−S cluster and the substrate and confirm that the difference in domain assembly across the two structures is a consequence of Fe−S cluster and substrate binding. The Fe−S cluster-bound but substrate- and inhibitor-free structure of LmFH showed increased mobility of the C-terminus domain as compared to the substrate/inhibitor-bound structure.[73] Since the pocket for the entry of the substrate to the active site lies between the α- and β-subunit interfaces, it is possible that the β-subunit mobility may regulate substrate entry/product exit into the active site by opening/closing during catalytic cycles.

The kinetic parameters obtained for the enzyme are in concordance with previous reports on class-I FHs. However, we observed substrate inhibition in this enzyme, which suggests an alternative binding site for the substrate. This is the first enzyme of this class to exhibit such a regulation with the only other known regulation reported in class-I FHs being cooperativity observed in *Trypanosoma cruzi*.[25] Interestingly, malonate, a known inhibitor of class-II FHs was bound to two different regions of the tunnel in LmFH, one at the entrance and the other at the center.[27] Two of the residues in the tunnel that bind to malonate in LmFH, Gln195 and Glu267 (LmFH numbering), are conserved, while Asp197 is present either as glutamate or as histidine in other class-I FHs. Residues Lys213 and Ser217 (part of the KGXGS motif) are close to the tunnel with Lys213 at around 10 Å from Gln195 and Glu267. An exhaustive search for side-chain rotamers of Lys213 followed by energy minimization in the LmFH structure reveals that the lysine residue comes in close contact of 4.5 Å from Glu267 (Figure 10). Mutating the lysine and serine residues results in significant changes in K_I (Table 1), suggesting that the alternative binding site in MjFH might also be located within the tunnel.

Recently, the first attempt at understanding the mechanism of catalysis in class-I FHs has been carried out in LmFH through mutational studies of active site residues. Residue Thr467 (LmFH numbering), closest to the C3 carbon of bound substrate, along with its hydrogen-bonded partners consisting of two arginyl residues, Arg421 and Arg471, has been predicted to act as a catalytic base, while Asp135 along with its hydrogen-bonded partner His334 performs the role of the catalytic acid.[73] Mutation of the predicted catalytic acid and base in LmFH led to a 2500−5500-fold decrease in activity (k_{cat}/K_M), while in MjFH, the corresponding mutations T80V and D62V led to a lower fall in activity (30−240-fold). It must be noted that the catalytic rate enhancement offered by the enzyme is of the order of 3×10^{15} and a 5000-fold decrease in the activity of the enzyme would still make it a phenomenal catalyst. This suggests that the rate-determining step in the fumarase reaction in the case of class-I FHs is not proton abstraction. We must therefore look

https://doi.org/10.1021/acs.biochem.2c00541
Biochemistry 2023, 62, 476−493

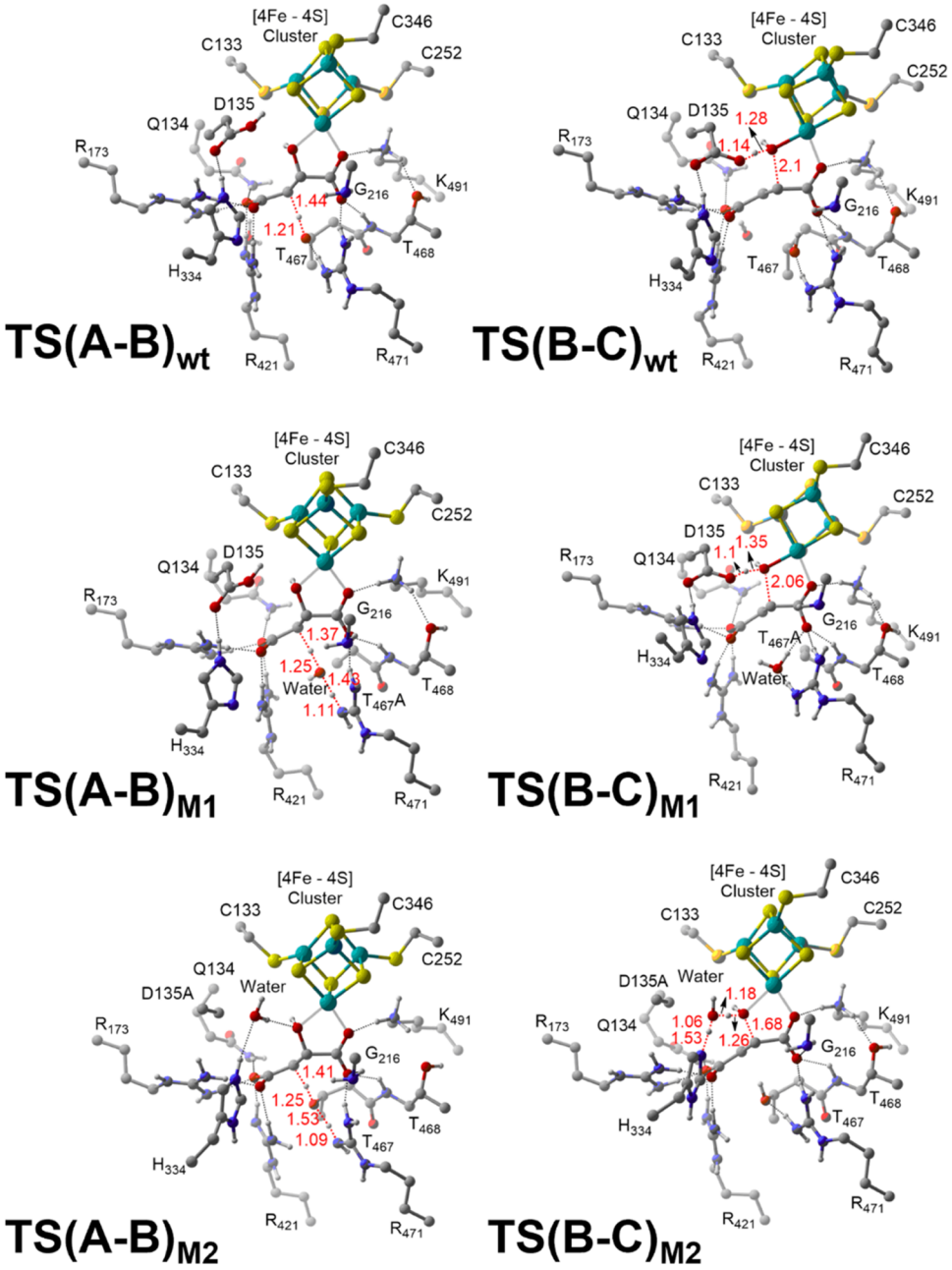

Figure 9. Optimized geometries of the two intermittent transition states obtained from QM2 in the wild-type enzyme (wt), T467A mutant (M1), and D135A mutant (M2). Distances shown are in Å.

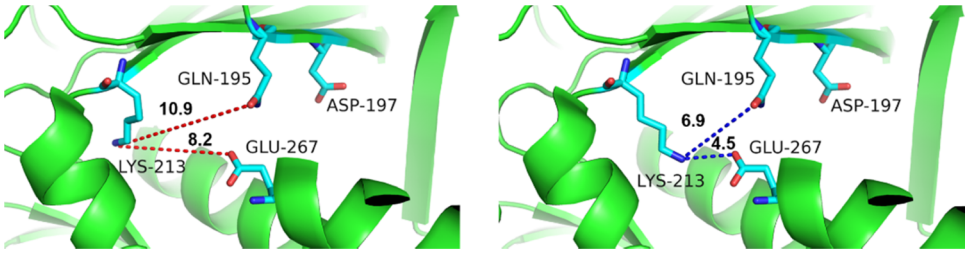

Figure 10. Contacts of Lys213 of the conserved KGXGS motif with Gln195 and Glu267 that interact with malonate bound at the tunnel in LmFH (5L2R). The panel on the left shows the interatomic distance between the Lys^{213} residue and Gln^{195} and Glu^{267} present in the tunnel. Search for possible side-chain rotamers of Lys^{213} in the same structure followed by energy minimization reveals that Lys^{213} comes close to Gln^{195} and Glu^{267}, as seen in the right panel. The tunnel in the LmFH structure is independent of the active site. The numbers above the dashed lines are distances in Å.

https://doi.org/10.1021/acs.biochem.2c00541
Biochemistry 2023, 62, 476−493

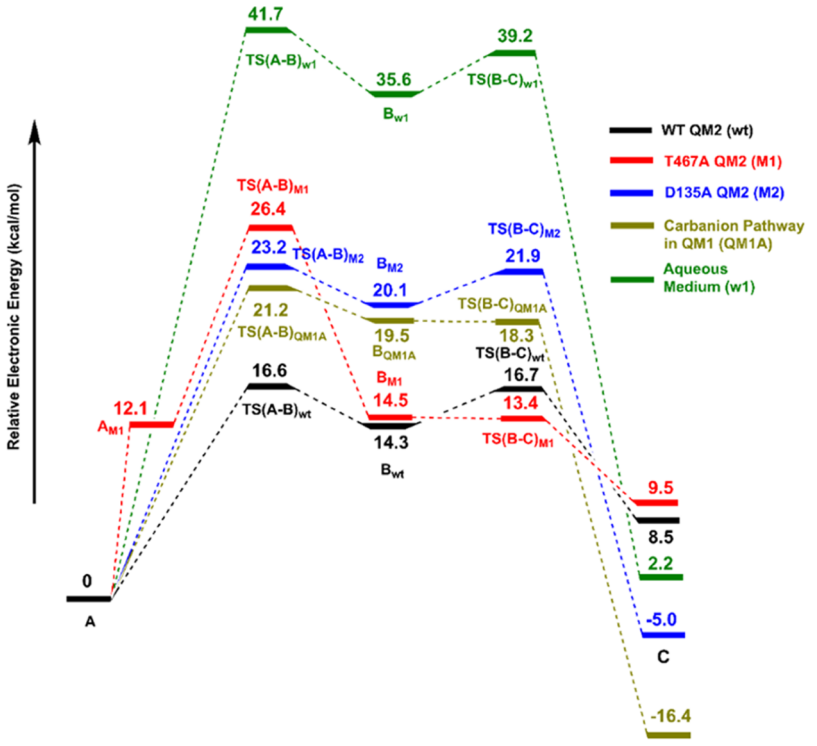

Figure 11. Electronic energy profiles obtained from different model systems.

elsewhere for the molecular origin of the large transition-state stabilization first noted by Bearne and Wolfenden.[4] Mutation of all of the residues (Gln61, Arg102, Gly147, Arg32, Thr81, and Arg84) that form a hydrogen-bonded network with the carboxylate groups of the substrate abolished activity in MjFH. These observations on the preferential loss of activity upon mutation of the substrate binding residues suggest the role of charge polarization in mediating catalysis in class-I FHs.

QM Calculation Supports Experimental Data Validating the Dominant Role of Substrate Charge Polarization in Catalysis. With the present studies on the catalytic mechanism in class-I FHs still in their nascent state, our understanding of this aspect is largely derived from studies carried out in class-II FHs. Though the biochemical equilibrium of the reaction catalyzed by FH is in the direction of fumarate to malate (K_{eq} = 4), the problem has been viewed in the light of dehydration rather than hydration. A serine residue has been identified as the catalytic base in class-II FHs, where it is believed to form an oxyanion hole, stabilized by interaction with positively charged neighbors. Previous studies, however, have revealed that the rate-limiting step does not involve a carbon−hydrogen bond cleavage, clearly suggesting that the reaction may not be driven largely through catalytic base-mediated proton abstraction.[74] Both class-I and class-II FHs catalyze the unidirectional hydration of acetylenedicarboxylate to oxaloacetate with good efficiencies.[75,76] This reaction, similar to the reaction catalyzed by acetylene hydratase, does not require a catalytic base, and the reaction is catalyzed by a water molecule held in a position bound to a tungsten cofactor. The bound water molecule is rendered nucleophilic or electrophilic by an aspartyl residue, thus allowing it to attack the triple bond.[77] In recent years, quantum chemical studies have proven successful in understanding the mechanism of enzymatic reactions. DFT calculations on both electrophilic and nucleophilic pathways for water attack on the triple bond of acetylene have shown very high energy barriers, suggesting an alternative mechanism in acetylene hydratases. We have carried out quantum chemical studies on class-I FHs to understand the mechanism that this enzyme adopts to catalyze the hydration/dehydration reaction of fumarate.

From our DFT calculations, we find that the carbanion pathway is the most favorable route of interconversion between malate and fumarate in aqueous medium as well as in the enzymatic active site. The uncatalyzed reaction in aqueous medium has a significant energy barrier (41.7 kcal mol^{-1}), which drastically goes down by 20.5 kcal mol^{-1} in the presence of the catalytic acid−base pair inside the protein environment (Figure 11). Incorporation of noncovalently interacting residues in the larger cluster QM2 results in further reduction of the energy barrier, suggesting that they might have an important role in the modification of the electronic structure of the substrate. A comparison of the TSs in aqueous solution and in the wt enzyme is warranted at this juncture. A closer look at both TSs, $\mathbf{TS(A-B)_{w1}}$ and $\mathbf{TS(A-B)_{wt}}$, clearly shows that the C−H bond distance is highly elongated (1.51 in $\mathbf{TS(A-B)_{w1}}$ and 1.44 in $\mathbf{TS(A-B)_{wt}}$; Figures 7 and 9). This elongation in the TS develops a significant carbanion character in the TS. While, in the aqueous solution, there is no stabilization of the carbanion, in the enzyme, the presence of adjacent residues stabilizes this negative charge, leading to huge TS stabilization.

A closer look at the active site of class-I FH reveals that the environment is polarized with more positively charged interaction at one end of the substrate than that at the other. We hypothesize that the active site environment polarizes the double bond of fumarate so that the nucleophilic attack of the hydroxyl group becomes favorable. To understand if the double bond of fumarate is really primed for the attack of the water molecule, we performed natural population analysis (NPA) calculation on the fumarate-bound enzyme−substrate

https://doi.org/10.1021/acs.biochem.2c00541
Biochemistry 2023, 62, 476−493

complex in the larger model, QM2 for WT and various mutants (Table 2). From the NPA calculation, it is observed

Table 2. NPA Charges on Bound Fumarate for Different Mutants of LmFH

mutant	NPA charge on C3	NPA charge on C2	relative NPA charge on C2 w.r.t. C3
WT	−0.306	−0.212	+0.094
R471A	−0.286	−0.222	+0.064
R421A	−0.265	−0.231	+0.034
R173A	−0.273	−0.212	+0.061
R421A + R173A	−0.237	−0.272	−0.035
R421A + R173A + R471A	−0.240	−0.294	−0.054
K491A	−0.314	−0.198	+0.116
D135A	−0.302	−0.234	+0.068
D135A + H334A	−0.275	−0.234	+0.041
Q134A	−0.318	−0.214	+0.104
T467A	−0.264	−0.228	+0.036
T468A	−0.282	−0.201	+0.081
G216A	−0.284	−0.223	+0.061
fumarate	−0.285	−0.285	0.000
fumarate + [4Fe−4S] cluster	−0.245	−0.286	−0.041

that the charge separation is maximum for WT with K491A and Q134A mutants being the only exceptions. As the active site residues are mutated, the relative charge separation reduces, making fumarate less nucleophilic, which can in turn cause an increase in activation energies as already observed in the case of T467A and D135A mutants. Importantly, active site arginine residues play a significant role in charge separation. As the three arginine residues are removed sequentially from the active site, charge separation not only reduces but the polarity completely gets reversed. Thus, the nucleophilicity of the substrate totally diminishes as the arginine residues are mutated, which in turn demolishes the enzyme activity. From the good correlation obtained here, it can be said that noncovalent interactions present at the active site of FH also have an essential part in making the enzyme more efficient by polarizing the substrate.

Proposed Mechanism of Catalysis in Class-I FHs. With the understanding that the base-mediated proton abstraction is not the rate-limiting step of the reaction and reduction in energy barriers is not achieved solely by the catalytic acid and base pair, the transition-state analogues have been used to explain the series of covalent changes that take place during the fumarase reaction of an enzyme-bound substrate.[15] Rate enhancements in enzymes take place by reducing the activation barrier of the reaction by binding strongly to the altered substrate in its transition state compared to the substrate in its ground state.[4] FH stabilizes this altered substrate in its transition state by a reduction in free energy by at least 30 kcal mol^{-1} with a release in enthalpy of −24 kcal mol^{-1} and a gain in entropy of 19 kcal mol^{-1}.[4] It is observed that the C3− carbanion intermediate binds FH very strongly, mimicking the transition state.[15] The large favorable enthalpy gain in the fumarase reaction clearly arises from the strong network of electrostatic interactions formed by the substrate at the preorganized active site. The importance of active site preorganization and the electrostatic origin of the catalytic power of enzymes has been well addressed by Warshel and co-workers.[78] To further support our hypothesis of preorganization in the active site, we superimposed the optimized geometries of reactant complex **A** with $\mathbf{TS(A-B)}_{wt}$ and intermediate $\mathbf{B}_{wt}$ with $\mathbf{TS(B-C)}_{wt}$. The images provided in the Supporting Information (Figures S17 and S18) show a very good overlap between the reactant and TSs, which in turn implies that there are fewer structural changes taking place on moving from the ground state to the TS. This clearly indicates that the active site is highly preorganized and therefore much less energy needs to be expended on moving to the TS. In the absence of the substrate, the charged active site residues are likely to be heavily hydrated. The binding of the dianionic substrate will be accompanied by a release of the hydration shells around both the positive side chain of enzymes and the negative charge of carboxylate groups of the substrate, contributing to a large gain in entropy.

The active site of class-II FH as well reveals a pattern similar to class-I FH, where the number of hydrogen bonds with the substrate is much larger on one end than that on the other (Figure 12). We hypothesize that polarization of the substrate

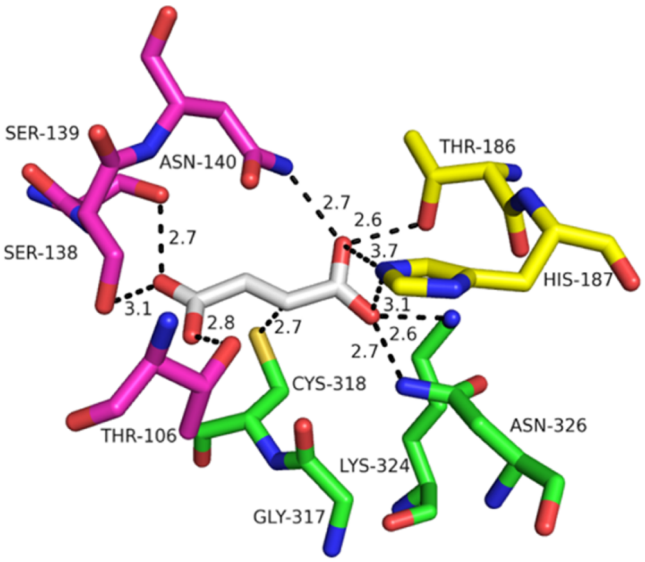

Figure 12. Active site architecture of class-II FH taken from *M. tuberculosis* FH reveals a larger number of H-bonds at one end of the substrate than that at the other. Residues from three subunits contribute to catalysis in class-II FH, labeled as magenta, green, and yellow. We see that while a serine and threonine residue are in H-bonding distance from the carboxylate group of the substrate (highlighted in gray) from one end, stronger interactions with lysine, histidine, and asparagine are observed on the other end. The numbers next to the dashed lines are distances in Å.

at the active site mediated by noncovalent interactions could potentially form the basis of catalysis where binding of the substrate and catalysis become inseparable events as predicted by the transition state theory. Upon substrate binding to the active site, the surrounding residues prime the substrate for nucleophilic attack and provide electrostatic stabilization to the negative charge on the carbanionic intermediate form of the substrate approaching the transition state (Figure 13). Bearne and Wolfenden had long predicted that the electrostatic stabilization could explain the large gain in entropy (19 kcal mol^{-1}) observed for binding the altered substrate in its transition state relative to the ground state.[4] It should be noted that to fully understand the transition-state stabilization, one also needs to calculate the binding free energy in the ground state by sampling the complete enzyme configurational space.

https://doi.org/10.1021/acs.biochem.2c00541
Biochemistry 2023, 62, 476−493

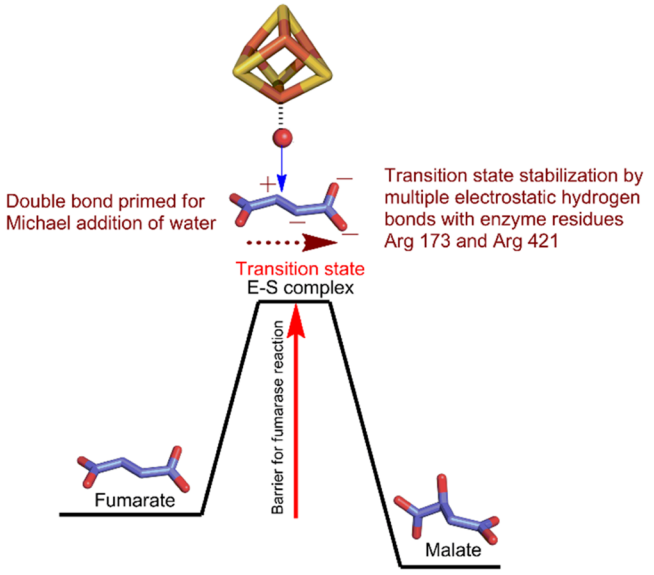

Figure 13. Mechanism of enzyme catalysis in FH. Upon binding to the active site of the enzyme, the substrate is raised to its transition state mediated by the positively charged residues on both sides of the substrate, strongly polarizing it. The transition state complex is well primed for the attack of a water molecule held in place by the Fe−S cluster, following which the product is released.

Fumarate hydratase could be considered an example of a true "Pauling enzyme".[79] The Fe−S cluster may have been retained as a part of enzyme evolution and only plays a nonredox role in holding the water molecule in place for catalysis, similar to that observed in the tungsten-containing enzyme, acetylene hydratase.[77] In the case of aconitase, a 4Fe−4S cluster containing hydrolyase, the Fe−S cluster is believed to act as a Lewis acid,[80] where the hydroxyl group of the substrate is rendered prone to cleavage. However, in the case of class-I FH, the Fe−S cluster holds a water molecule in place for the hydration reaction, as the enzyme is more a hydratase than a dehydratase with the K_{eq} of the reaction greater by 4-fold in the direction of hydration.[5,6] Preorganized polar environments of active sites have been invoked to drive enzymatic catalysis through electrostatic stabilization of the substrate.[81] Recent studies on ketosteroid isomerase, which is an exceptional enzyme that stabilizes the substrate in the transition state by 21 kcal mol^{-1}, have shown the role of the electrostatic field at the active site on enzyme catalysis.[82,83] Using vibrational stark effect spectroscopy, it was observed that the electrostatic field at the active site contributes significantly to the reduction in the free energy barrier and subsequently its catalytic rate. Of the 11.5 kcal mol^{-1} activation barrier, a reduction of 7.3 kcal mol^{-1}, which corresponds to 70% of the enzyme catalytic rate compared to the uncatalyzed reaction, was attributed to the electrostatic field alone. Positioning of the catalytic base, an aspartate residue, contributed to the rest of the catalytic rate enhancement.[83] Probing enzymes for electric field effects as a criterion for rate enhancements can provide useful insights into some of the exceptional enzymes in nature that carry out reactions at enormous rates, which otherwise would not have been possible.

CONCLUSIONS

The extraordinary proficiency of fumarate hydratases in catalyzing the stereospecific addition of water to the planar, symmetrical, and dianionic substrate, fumarate, is in large measure due to the constellation of positively charged residues that line the preorganized active site, polarizing the substrate electron distribution such that in the transition state, the olefinic double bond distorts to the aci-carboxylate form. Dramatic electrostatic stabilization of transition states in enzyme catalysis is provided by the example of ketosteroid isomerase, where the activation barrier is reduced by an estimated 21 kcal mol^{-1}. Fumarate hydratases may provide an even more extreme example of transition-state stabilization, envisaged decades ago by Polanyi, Haldane, and Pauling and elaborated in later years by the seminal work of Jencks.[79,84−86] Extensive computational studies by Warshel and co-workers have provided sufficient evidence in favor of these proposals that have led to a better understanding of the origin of enzyme catalysis.[81,87,88] The studies described above also provide firm experimental and theoretical support for the molecular mechanisms that enable fumarate hydratases to bear the energetic burden of catalysis clearly enunciated in the work of Bearne and Wolfenden.[4]

ASSOCIATED CONTENT

Supporting Information

The Supporting Information is available free of charge at https://pubs.acs.org/doi/10.1021/acs.biochem.2c00541.

Additional experimental details, materials, and methods; modeling of missing residues/fragments in MjFH and LmFH for MD simulations; docking the 4Fe−4S cluster into apo-MjFH; metadynamics simulation of holo-MjFH; variations between apo- and holo-forms of MjFH and LmFH; quantum chemical calculations on the reaction mechanism of fumarate hydration in solution and at the enzyme active site; and Cartesian coordinates (PDF)

Accession Codes

UniProt ID: MjFH α-subunit: Q58690, MjFH β-subunit: Q58034.

AUTHOR INFORMATION

Corresponding Authors

Garima Jindal − *Department of Organic Chemistry, Indian Institute of Science, Bengaluru 560012, India;* orcid.org/0000-0002-5766-935X; Phone: +91-80-22932689; Email: gjindal@iisc.ac.in

Hemalatha Balaram − *Molecular Biology and Genetics Unit, Jawaharlal Nehru Centre for Advanced Scientific Research, Bengaluru 560064, India;* orcid.org/0000-0002-8821-1288; Phone: +91-80-22082812; Email: hb@jncasr.ac.in

Authors

Asutosh Bellur − *Molecular Biology and Genetics Unit, Jawaharlal Nehru Centre for Advanced Scientific Research, Bengaluru 560064, India*

Soumik Das − *Department of Organic Chemistry, Indian Institute of Science, Bengaluru 560012, India;* Present Address: Department of Chemistry, University of Michigan, 930 North University Avenue, Ann Arbor, Michigan 48109-1055, United States; orcid.org/0000-0002-1951-1906

Vijay Jayaraman − *Molecular Biology and Genetics Unit, Jawaharlal Nehru Centre for Advanced Scientific Research, Bengaluru 560064, India;* Present Address: Department of

https://doi.org/10.1021/acs.biochem.2c00541
Biochemistry 2023, 62, 476−493

Molecular Cell Biology, Weizmann Institute of Science, Rehovot 7610001, Israel

Sudarshan Behera − *Chemistry and Physics of Materials Unit, Jawaharlal Nehru Centre for Advanced Scientific Research, Bengaluru 560064, India;* orcid.org/0000-0003-1025-0639

Arpitha Suryavanshi − *Molecular Biology and Genetics Unit, Jawaharlal Nehru Centre for Advanced Scientific Research, Bengaluru 560064, India*

Sundaram Balasubramanian − *Chemistry and Physics of Materials Unit, Jawaharlal Nehru Centre for Advanced Scientific Research, Bengaluru 560064, India;* orcid.org/0000-0002-3355-6764

Padmanabhan Balaram − *National Centre for Biological Sciences, Bengaluru 560065, India;* orcid.org/0000-0002-6577-933X

Complete contact information is available at: https://pubs.acs.org/10.1021/acs.biochem.2c00541

Author Contributions

[▽]A.B. and S.D. contributed equally to this work.

Author Contributions

A.B.: structure solution of MjFH full-length apo-protein, construction of MjFH site-directed mutants, kinetics of MjFH wild type and mutants, structure analysis, interpretation of data, and manuscript writing; V.J.: cloning of MjFH and heterologous expression, purification, activity measurements, structure solution of the MjFH β-subunit and full-length apo-protein, and biochemical characterization; A.S.: generation of site-directed mutants; S.D. and G.J.: computation: DFT and natural population analysis, and manuscript writing; S. Behera and S. Balasubramanian: computation: MD simulation and metadynamics, and manuscript writing; P.B.: conceptualization, structure analysis, and manuscript writing; and H.B.: funding, conceptualization, interpretation and analysis of all data, and manuscript writing.

Notes

The authors declare no competing financial interest.

All data described in the article are contained within the article/Supporting Information. MjFH$\alpha\beta$ apo-protein complex (7XKY) and MjFHβ protein (5DNI) structures are deposited and available in the RCSB database.

■ ACKNOWLEDGMENTS

The diffraction data for MjFHβ were collected at the X-ray facility at the Molecular Biophysics Unit, Indian Institute of Science, Bengaluru, India, and data for Apo-MjFH$\alpha\beta$ were collected at the BM-14 beamline of the European Synchrotron Radiation Facility (ESRF), Grenoble, France. The authors acknowledge the assistance of Jyothi Kunala with analytical size exclusion chromatography. H.B. acknowledges financial support from the Department of Biotechnology, Ministry of Science and Technology, Government of India Grants BT/PR11294/BRB/10/1291/2014, BT/PR13760/COE/34/42/2015, and BT/INF/22/SP27679/2018; Science and Engineering Research Board (SERB), Department of Science and Technology, Government of India Grant CRG/2019/004150/IBS, EMR/2014/001276; JC Bose Fellowship, SERB; and institutional funding from JNCASR. G.J. acknowledges the funding (SRG/2019/001646) from the Science and Engineering Research Board (SERB). Computing time from Supercomputer Education and Research Centre (SERC), IISc, Bangalore is also gratefully acknowledged. S. Behera thanks CSIR for the fellowship and S. Behera and S. Balasubramanian gratefully acknowledge the support and the resources provided by the "PARAM Yukti Facility" under the National Supercomputing Mission, Government of India at the Jawaharlal Nehru Centre For Advanced Scientific Research. A.B. was supported by CSIR for junior and senior research fellowships and from the JC Bose fellowship awarded to H.B.

■ ABBREVIATIONS

FH, fumarate hydratase; Mj, *Methanocaldococcus jannaschii*; Lm, *Leishmania major*; DFT, density functional theory; NPA, natural population analysis; MD, molecular dynamics; NTD, N-terminal domain; CTD, C-terminal domain

■ REFERENCES

(1) Jin, J.; Hanefeld, U. The selective addition of water to C≡C bonds; enzymes are the best chemists. *Chem. Commun.* **2011**, *47*, 2502−2510.

(2) Chen, B. S.; Otten, L. G.; Hanefeld, U. Stereochemistry of enzymatic water addition to C=C bonds. *Biotechnol. Adv.* **2015**, *33*, 526−546.

(3) Resch, V.; Hanefeld, U. The selective addition of water. *Catal. Sci. Technol.* **2015**, *5*, 1385−1399.

(4) Bearne, S. L.; Wolfenden, R. Enzymatic Hydration of an Olefin: The Burden Borne by Fumarase. *J. Am. Chem. Soc.* **1995**, *117*, 9588−9589.

(5) Krebs, H. A. The equilibrium constants of the fumarase and aconitase systems. *Biochem. J.* **1953**, *54*, 78−82.

(6) Goldberg, R. N.; Tewari, Y. B. Thermodynamics of Enzyme-Catalyzed Reactions: Part 4. Lyases. *J. Phys. Chem. Ref. Data* **1995**, *24*, 1669−1698.

(7) Erickson, B. L. E.; Alberty, R. A. Kinetics and mechanism of the base-catalyzed hydration of fumarate to malate. *J. Phys. Chem. A* **1959**, *63*, 705−709.

(8) Gajewski, E.; Goldberg, R. N.; Steckler, D. K. Thermodynamics of the conversion of fumarate to L-(-)-malate. *Biophys. Chem.* **1985**, *22*, 187−195.

(9) Woods, S. A.; Schwartzbach, S. D.; Guest, J. R. Two biochemically distinct classes of fumarase in *Escherichia coli*. *Biochim. Biophys. Acta, Protein Struct. Mol. Enzymol.* **1988**, *954*, 14−26.

(10) Jayaraman, V.; Suryavanshi, A.; Kalale, P.; Kunala, J.; Balaram, H. Biochemical characterization and essentiality of *Plasmodium fumarate* hydratase. *J. Biol. Chem.* **2018**, *293*, 5878−5894.

(11) Kronen, M.; Berg, I. A. Mesaconase/fumarase FumD in *Escherichia coli* O157:H7 and promiscuity of *Escherichia coli* class i fumarases FumA and FumB. *PLoS One* **2015**, *10*, No. e0145098.

(12) Hansen, J. N.; Dinovo, E. C.; Boyer, P. D. Initial and equilibrium 18O, 14C, 3H, and 2H exchange rates as probes of the fumarase reaction mechanism. *J. Biol. Chem.* **1969**, *244*, 6270−6279.

(13) Blanchard, J. S.; Cleland, W. W. Use of Isotope Effects To Deduce the Chemical Mechanism of Fumarase. *Biochemistry* **1980**, *19*, 4506−4513.

(14) Rose, I. A. How fumarase recycles after the malate - Fumarate reaction. Insights into the reaction mechanism. *Biochemistry* **1998**, *37*, 17651−17658.

(15) Porter, D. J.; Bright, H. J. 3-Carbanionic substrate analogues bind very tightly to fumarase and aspartase. *J. Biol. Chem.* **1980**, *255*, 4772−4780.

(16) Puthan Veetil, V.; Fibriansah, G.; Raj, H.; Thunnissen, A.-M. W. H.; Poelarends, G. J. Aspartase/fumarase superfamily: A common catalytic strategy involving general base-catalyzed formation of a highly stabilized aci - Carboxylate intermediate. *Biochemistry* **2012**, *51*, 4237−4243.

(17) Sweet, W. L.; Blanchard, J. S. Fumarase: Viscosity dependence of the kinetic parameters. *Arch. Biochem. Biophys.* **1990**, *277*, 196−202.

(18) Rose, I. A.; Warms, J. V. B.; Kuo, D. J. Proton Transfer in Catalysis by Fumarase. *Biochemistry* **1992**, *31*, 9993−9999.
(19) Rose, I. A.; Warms, J. V. B.; Yuan, R. G. Role of Conformational Change in the Fumarase Reaction Cycle. *Biochemistry* **1993**, *32*, 8504−8511.
(20) Shimoyama, T.; Rajashekhara, E.; Ohmori, D.; Kosaka, T.; Watanabe, K. MmcBC in *Pelotomaculum thermopropionicum* represents a novel group of prokaryotic fumarases. *FEMS Microbiol. Lett.* **2007**, *270*, 207−213.
(21) van Vugt-Lussenburg, B. M. A.; van der Weel, L.; Hagen, W. R.; Hagedoorn, P. L. Biochemical Similarities and Differences between the Catalytic [4Fe-4S] Cluster Containing Fumarases FumA and FumB from *Escherichia coli*. *PLoS One* **2013**, *8*, No. e55549.
(22) Shibata, H.; Gardiner, W. E.; Schwartzbach, S. D. Purification, characterization, and immunological properties of fumarase from *Euglena gracilis* var. bacillaris. *J. Bacteriol.* **1985**, *164*, 762−768.
(23) Kuijk, B. L.; Stams, A. J. M. Purification and characterization of malate dehydrogenase from the syntrophic propionate-oxidizing bacterium strain MPOB. *FEMS Microbiol. Lett.* **1996**, *144*, 141−144.
(24) Kronen, M.; Sasikaran, J.; Berg, I. A. Mesaconase activity of class I fumarase contributes to mesaconate utilization by *Burkholderia xenovorans*. *Appl. Environ. Microbiol.* **2015**, *81*, 5632−5638.
(25) de Pádua, R. A.; Kia, A. M.; Costa-Filho, A. J.; Wilkinson, S. R.; Nonato, M. C. Characterisation of the fumarate hydratase repertoire in *Trypanosoma cruzi*. *Int. J. Biol. Macromol.* **2017**, *102*, 42−51.
(26) Feliciano, P. R.; Gupta, S.; Dyszy, F.; Dias-Baruffi, M.; Costa-Filho, A. J.; Michels, P. A. M.; Nonato, M. C. Fumarate hydratase isoforms of *Leishmania major*: Subcellular localization, structural and kinetic properties. *Int. J. Biol. Macromol.* **2012**, *51*, 25−31.
(27) Feliciano, P. R.; Drennan, C. L.; Nonato, M. C. Crystal structure of an Fe-S cluster-containing fumarate hydratase enzyme from *Leishmania major* reveals a unique protein fold. *Proc. Natl. Acad. Sci. U.S.A.* **2016**, *113*, 9804−9809.
(28) van Vugt-Lussenburg, B. M. A.; van der Weel, L.; Hagen, W. R.; Hagedoorn, P. L. Identification of two [4Fe-4S]-cluster-containing hydro-lyases from *Pyrococcus furiosus*. *Microbiology* **2009**, *155*, 3015−3020.
(29) Sambrook, J.; Russell, D. W. *Molecular Cloning—Sambrook & Russel—Vol. 1, 2, 3*; CSH Press, 2001.
(30) Bradford, M. M. A rapid and sensitive method for the quantitation of microgram quantities of protein utilizing the principle of protein-dye binding. *Anal. Biochem.* **1976**, *72*, 248−254.
(31) Beinert, H.; Kennedy, M. C.; Stout, C. D. Aconitase as Iron−Sulfur Protein, Enzyme, and Iron-Regulatory Protein. *Chem. Rev.* **1996**, *96*, 2335−2374.
(32) Yano, T.; Sled', V. D.; Ohnishi, T.; et al. Expression and characterization of the flavoprotein subcomplex composed of 50-kDa (NQO1) and 25-kDa (NQO2) subunits of the proton-translocating NADH-quinone oxidoreductase of *Paracoccus denitrificans*. *J. Biol. Chem.* **1996**, *271*, 5907−5913.
(33) Chayen, N. E.; Shaw Stewart, P. D.; Blow, D. M. Microbatch crystallization under oil - a new technique allowing many small-volume crystallization trials. *J. Cryst. Growth* **1992**, *122*, 176−180.
(34) Winn, M. D.; Ballard, C. C.; Cowtan, K. D.; Dodson, E. J.; Emsley, P.; Evans, P. R.; Keegan, R. M.; Krissinel, E. B.; Leslie, A. G. W.; McCoy, A.; McNicholas, S. J.; Murshudov, G. N.; Pannu, N. S.; Potterton, E. A.; Powell, H. R.; Read, R. J.; Vagin, A.; Wilson, K. S. Overview of the CCP4 suite and current developments. *Acta Crystallogr., Sect. D: Biol. Crystallogr.* **2011**, *67*, 235−242.
(35) Adams, P. D.; Afonine, P. V.; Bunkóczi, G.; Chen, V. B.; Davis, I. W.; Echols, N.; Headd, J. J.; Hung, L. W.; Kapral, G. J.; Grosse-Kunstleve, R. W.; McCoy, A. J.; Moriarty, N. W.; Oeffner, R.; Read, R. J.; Richardson, D. C.; Richardson, J. S.; Terwilliger, T. C.; Zwart, P. H. PHENIX: A comprehensive Python-based system for macromolecular structure solution. *Acta Crystallogr., Sect. D: Biol. Crystallogr.* **2010**, *66*, 213−221.
(36) Battye, T. G. G.; Kontogiannis, L.; Johnson, O.; Powell, H. R.; Leslie, A. G. W. iMOSFLM: A new graphical interface for diffraction-image processing with MOSFLM. *Acta Crystallogr., Sect. D: Biol. Crystallogr.* **2011**, *67*, 271−281.
(37) Evans, P. Scaling and assessment of data quality. *Acta Crystallogr., Sect. D: Biol. Crystallogr.* **2006**, *62*, 72−82.
(38) McCoy, A. J.; Grosse-Kunstleve, R. W.; Adams, P. D.; Winn, M. D.; Storoni, L. C.; Read, R. J. Phaser crystallographic software. *J. Appl. Crystallogr.* **2007**, *40*, 658−674.
(39) Terwilliger, T. C.; Grosse-Kunstleve, R. W.; Afonine, P. V.; Moriarty, N. W.; Zwart, P. H.; Hung, L. W.; Read, R. J.; Adams, P. D. Iterative model building, structure refinement and density modification with the PHENIX AutoBuild wizard. *Acta Crystallogr., Sect. D: Biol. Crystallogr.* **2008**, *64*, 61−69.
(40) Murshudov, G. N.; Skubák, P.; Lebedev, A. A.; Pannu, N. S.; Steiner, R. A.; Nicholls, R. A.; Winn, M. D.; Long, F.; Vagin, A. A. REFMAC5 for the refinement of macromolecular crystal structures. *Acta Crystallogr., Sect. D: Biol. Crystallogr.* **2011**, *67*, 355−367.
(41) Afonine, P. V.; Grosse-Kunstleve, R. W.; Echols, N.; Headd, J. J.; Moriarty, N. W.; Mustyakimov, M.; Terwilliger, T. C.; Urzhumtsev, A.; Zwart, P. H.; Adams, P. D. Towards automated crystallographic structure refinement with phenix.refine. *Acta Crystallogr., Sect. D: Biol. Crystallogr.* **2012**, *68*, 352−367.
(42) Emsley, P.; Lohkamp, B.; Scott, W. G.; Cowtan, K. Features and development of Coot. *Acta Crystallogr., Sect. D: Biol. Crystallogr.* **2010**, *66*, 486−501.
(43) Schrödinger. *The PyMOL Molecular Graphics System*; Schrödinger LLC, 2015; Vol. *26*, pp 708−715.
(44) Baker, N. A.; Sept, D.; Joseph, S.; Holst, M. J.; McCammon, J. A. Electrostatics of nanosystems: Application to microtubules and the ribosome. *Proc. Natl. Acad. Sci. U.S.A.* **2001**, *98*, 10037−10041.
(45) Laio, A.; Parrinello, M. Escaping free-energy minima. *Proc. Natl. Acad. Sci. U.S.A.* **2002**, *99*, 12562−12566.
(46) Huang, J.; Rauscher, S.; Nawrocki, G.; Ran, T.; Feig, M.; de Groot, B. L.; Grubmuller, H.; MacKerell, A. D., Jr CHARMM36m: an improved force field for folded and intrinsically disordered proteins. *Nat. Methods* **2017**, *14*, 71−73.
(47) Vanommeslaeghe, K.; Hatcher, E.; Acharya, C.; Kundu, S.; Zhong, S.; Shim, J.; Darian, E.; Guvench, O.; Lopes, P.; Vorobyov, I.; MacKerell, A. D., Jr. CHARMM general force field: A force field for drug-like molecules compatible with the CHARMM all-atom additive biological force fields. *J. Comput. Chem.* **2010**, *31*, 671−690.
(48) Chang, C. H.; Kim, K. Density functional theory calculation of bonding and charge parameters for molecular dynamics studies on [FeFe] hydrogenases. *J. Chem. Theory Comput.* **2009**, *5*, 1137−1145.
(49) Berendsen, H. J. C.; van der Spoel, D.; van Drunen, R. GROMACS: A message-passing parallel molecular dynamics implementation. *Comput. Phys. Commun.* **1995**, *91*, 43−56.
(50) Frisch, M. J.; Trucks, G. W.; Schlegel, H. B.; Scuseria, G. E.; Robb, M. A.; Cheeseman, J. R.; Scalmani, G.; Barone, V.; Petersson, G. A.; Nakatsuji, H.; Li, X.; Caricato, M.; Marenich, A.; Bloino, J.; Janesko, B. G.; Gomperts, R.; Mennucci, B.; Hratchian, H. P.; Ortiz, J. V.; Izmaylov, A. F.; Sonnenberg, J. L.; Williams-Young, D.; Ding, F.; Lipparini, F.; Egidi, F.; Goings, J.; Peng, B.; Petrone, A.; Henderson, T.; Ranasinghe, D.; Zakrzewski, V. G.; Gao, J.; Rega, N.; Zheng, G.; Liang, W.; Hada, M.; Ehara, M.; Toyota, K.; Fukuda, R.; Hasegawa, J.; Ishida, M.; Nakajima, T.; Honda, Y.; Kitao, O.; Nakai, H.; Vreven, T.; Throssell, K.; Montgomery, J. A., Jr.; Peralta, J. E.; Ogliaro, F.; Bearpark, M.; Heyd, J. J.; Brothers, E.; Kudin, K. N.; Staroverov, V. N.; Keith, T.; Kobayashi, R.; Normand, J.; Raghavachari, K.; Rendell, A.; Burant, J. C.; Iyengar, S. S.; Tomasi, J.; Cossi, M.; Millam, J. M.; Klene, M.; Adamo, C.; Cammi, R.; Ochterski, J. W.; Martin, R. L.; Morokuma, K.; Farkas, O.; Foresman, J. B.; Fox, D. J. *Gaussian 09*, revision A.02; Gaussian, Inc.: Wallingford, CT, 2016.
(51) Lee, C.; Yang, W.; Parr, R. G. Development of the Colle-Salvetti correlation-energy formula into a functional of the electron density. *Phys. Rev. B* **1988**, *37*, 785.
(52) Becke, A. D. Density-functional thermochemistry. III. The role of exact exchange. *J. Chem. Phys.* **1993**, *98*, 5648.
(53) Hehre, W. J.; Lathan, W. A. Self-Consistent Molecular Orbital Methods. XIV. An Extended Gaussian-Type Basis for Molecular

https://doi.org/10.1021/acs.biochem.2c00541
Biochemistry 2023, 62, 476−493

Orbital Studies of Organic Molecules. Inclusion of Second Row Elements. *J. Chem. Phys.* **1972**, *56*, 5255.
(54) Hariharan, P. C.; Pople, J. A. The influence of polarization functions on molecular orbital hydrogenation energies. *Theor. Chim. Acta* **1973**, *28*, 213−222.
(55) Hay, P. J.; Wadt, W. R. Ab initio effective core potentials for molecular calculations. Potentials for K to Au including the outermost core orbitals. *J. Chem. Phys.* **1985**, *82*, 299.
(56) Fukui, K. The Path of Chemical Reactions - The IRC Approach. *Acc. Chem. Res.* **1981**, *14*, 363−368.
(57) Hratchian, H. P.; Schlegel, H. B. Finding Minima, Transition States, and following Reaction Pathways on Ab Initio Potential Energy Surfaces. In *Theory and Applications of Computational Chemistry*; Elsevier B.V., 2005; pp 195−249.
(58) Gonzalez, C.; Bernhard Schlegel, H. An improved algorithm for reaction path following. *J. Chem. Phys.* **1989**, *90*, 2154.
(59) Gonzalez, C.; Schlegel, H. B. Reaction path following in mass-weighted internal coordinates. *J. Phys. Chem. B* **1990**, *94*, 5523−5527.
(60) Grimme, S.; Ehrlich, S.; Goerigk, L. Effect of the damping function in dispersion corrected density functional theory. *J. Comput. Chem.* **2011**, *32*, 1456−1465.
(61) Marenich, A. V.; Cramer, C. J.; Truhlar, D. G. Universal solvation model based on solute electron density and on a continuum model of the solvent defined by the bulk dielectric constant and atomic surface tensions. *J. Phys. Chem. B* **2009**, *113*, 6378−6396.
(62) Siegbahn, P. E. M.; Crabtree, R. H. Mechanism of C-H activation by diiron methane monooxygenases: Quantum chemical studies. *J. Am. Chem. Soc.* **1997**, *119*, 3103−3113.
(63) Filatov, M.; Harris, N.; Shaik, S. On the "Rebound" Mechanism of Alkane Hydroxylation by Cytochrome P450: Electronic Structure of the Intermediate and the Electron Transfer Character in the Rebound Step. *Angew. Chem., Int. Ed.* **1999**, *38*, 3510.
(64) Basch, H.; Mogi, K.; Musaev, D. G.; Morokuma, K. Mechanism of the methane → methanol conversion reaction catalyzed by methane monooxygenase: A density functional study. *J. Am. Chem. Soc.* **1999**, *121*, 7249−7256.
(65) Wirstam, M.; Blomberg, M. R. A.; Siegbahn, P. E. M. Reaction mechanism of compound I formation in heme peroxidases: A density functional theory study. *J. Am. Chem. Soc.* **1999**, *121*, 10178−10185.
(66) Blomberg, M. R. A.; Borowski, T.; Himo, F.; Liao, R. Z.; Siegbahn, P. E. M. Quantum chemical studies of mechanisms for metalloenzymes. *Chem. Rev.* **2014**, *114*, 3601−3658.
(67) Himo, F. Recent Trends in Quantum Chemical Modeling of Enzymatic Reactions. *J. Am. Chem. Soc.* **2017**, *139*, 6780−6786.
(68) Kazemi, M.; Himo, F.; Åqvist, J. Enzyme catalysis by entropy without Circe effect. *Proc. Natl. Acad. Sci. U.S.A.* **2016**, *113*, 2406−2411.
(69) Stephens, P. J.; Thomson, A. J.; Dunn, J. B.; Keiderling, T. A.; Rawlings, J.; Rao, K. K.; Hall, D. O. Circular dichroism and magnetic circular dichroism of iron-sulfur proteins. *Biochemistry* **1978**, *17*, 4770−4778.
(70) Fox, N. K.; Brenner, S. E.; Chandonia, J. M. SCOPe: Structural Classification of Proteins - Extended, integrating SCOP and ASTRAL data and classification of new structures. *Nucleic Acids Res.* **2014**, *42*, D304−D309.
(71) Feliciano, P. R.; Drennan, C. L.; Nonato, M. C. Crystal structures of fumarate hydratases from *Leishmania major* in a complex with inhibitor 2-thiomalate Crystal structures of fumarate hydratases from *Leishmania major* in a complex with inhibitor 2-thiomalate. *ACS Chem. Biol.* **2019**, *14*, 266−275.
(72) Bulusu, V.; Srinivasan, B.; Bopanna, M. P.; Balaram, H. Elucidation of the substrate specificity, kinetic and catalytic mechanism of adenylosuccinate lyase from *Plasmodium falciparum*. *Biochim. Biophys. Acta, Proteins Proteomics* **2009**, *1794*, 642−654.
(73) Feliciano, P. R.; Drennan, C. L. Structural and Biochemical Investigations of the [4Fe-4S] Cluster-Containing Fumarate Hydratase from *Leishmania major*. *Biochemistry* **2019**, *58*, 5011−5021.
(74) Bearne, S. L.; Wolfenden, R. Mandelate racemase in pieces: Effective concentrations of enzyme functional groups in the transition state. *Biochemistry* **1997**, *36*, 1646−1656.
(75) Flint, D. H. Initial kinetic and mechanistic characterization of *Escherichia coli* fumarase A. *Arch. Biochem. Biophys.* **1994**, *311*, 509−516.
(76) Teipel, J. W.; Hass, G. M.; Hill, R. L. The substrate specificity of fumarase. *J. Biol. Chem.* **1968**, *243*, 5684−5694.
(77) Seiffert, G. B.; Ullmann, G. M.; Messerschmidt, A.; Schink, B.; Kroneck, P. M. H.; Einsle, O. Structure of the non-redox-active tungsten/[4Fe:4S] enzyme acetylene hydratase. *Proc. Natl. Acad. Sci. U.S.A.* **2007**, *104*, 3073−3077.
(78) Warshel, A. Electrostatic origin of the catalytic power of enzymes and the role of preorganized active sites. *J. Biol. Chem.* **1998**, *273*, 27035−27038.
(79) Pauling, L. Molecular architecture and biological reactions. *Chem. Eng. News Arch.* **1946**, *24*, 1375−1377.
(80) Flint, D. H.; Allen, R. M. Iron-sulfur proteins with nonredox functions. *Chem. Rev.* **1996**, *96*, 2315−2334.
(81) Warshel, A.; Sharma, P. K.; Kato, M.; Xiang, Y.; Liu, H.; Olsson, M. H. M. Electrostatic basis for enzyme catalysis. *Chem. Rev.* **2006**, *106*, 3210−3235.
(82) Kamerlin, S. C. L.; Sharma, P. K.; Chu, Z. T.; Warshel, A. Ketosteroid isomerase provides further support for the idea that enzymes work by electrostatic preorganization. *Proc. Natl. Acad. Sci. U.S.A.* **2010**, *107*, 4075−4080.
(83) Fried, S. D.; Bagchi, S.; Boxer, S. G. Extreme electric fields power catalysis in the active site of ketosteroid isomerase. *Science* **2014**, *346*, 1510−1514.
(84) Robinson, P. J.; Holbrook, K. A. On adsorption catalysis. *Z. Electrochem.* **1972**, *27*, 142.
(85) Haldane, J. *Enzymes*; MIT Press, 2003; p 235.
(86) Jencks, W. *Catalysis in Chemistry and Enzymology*, 2nd ed.; Dover Publications Inc., 1987.
(87) Adamczyk, A. J.; Cao, J.; Kamerlin, S. C. L.; Warshel, A. Catalysis by dihydrofolate reductase and other enzymes arises from electrostatic preorganization, not conformational motions. *Proc. Natl. Acad. Sci. U.S.A.* **2011**, *108*, 14115−14120.
(88) Štrajbl, M.; Shurki, A.; Kato, M.; Warshel, A. Apparent NAC effect in chorismate mutase reflects electrostatic transition state stabilization. *J. Am. Chem. Soc.* **2003**, *125*, 10228−10237.

https://doi.org/10.1021/acs.biochem.2c00541
Biochemistry 2023, 62, 476−493